Tracer stirring and variability in the Antarctic Circumpolar Current near the Southwest Indian Ridge

Dhruv Balwada[1], Alison R. Gray[2], Lilian A. Dove[3], and Andrew F. Thompson[3]

[1]Lamont-Doherty Earth Observatory, Columbia University, Palisades, NY, USA
[2]School of Oceanography, University of Washington, Seattle, WA, USA
[3]Division of Geological and Planetary Sciences, Environmental Science and Engineering, California Institute of Technology, Pasadena, CA, USA

Key Points:

- Glider observations were used to analyze tracer structure at scales ≤ 100 km in the Antarctic Circumpolar Current.
- The vertical structure of density variance in the mixed layer (ML) is suggestive of ML instabilities and eddies.
- Small-scale flows contribute to stirring in the interior, as indicated by interior passive tracer structure.

Corresponding author: Dhruv Balwada, dbalwada@ldeo.columbia.edu

Abstract

Oceanic macroturbulence is efficient at stirring and transporting tracers. The dynamical properties of this stirring can be characterized by statistically quantifying tracer structures. Here, we characterize the macroscale (1-100 km) tracer structures observed by two Seagliders downstream of the Southwest Indian Ridge (SWIR) in the Antarctic Circumpolar Current (ACC). These are some of the first glider observations in an energetic standing meander of the ACC, regions associated with enhanced ventilation. The small-scale density variance in the mixed layer (ML) was relatively enhanced near the surface and base of the ML, while being muted in the middle, suggesting the formation mechanism to be associated to ML instabilities and eddies. In addition, ML density fronts were formed by comparable contributions from temperature and salinity gradients, suggesting the dominant role of stirring, over air-sea interactions, in their formation and sustainability. In the interior, along-isopycnal spectra and structure functions of spice indicated that there is relatively lower variance at smaller scales than would be expected based on non-local stirring, suggesting that flows smaller than the deformation radius play a role in the cascade of tracers to small scales. These interior spice anomalies spanned across isopycnals, and were found to be about 3-5 times flatter than the aspect ratio that would be expected for O(1) Burger number flows like interior QG dynamics, suggesting the ratio of vertical shear to horizontal strain is greater than N/f. This further supports that small-scale flows, with high-mode vertical structures, stir tracers and impact tracer distributions.

Plain Language Summary

Ocean eddies and fronts are efficient at stirring and generating tracer structures spanning a wide range of scales. This stirring is important for uptake of tracers, particularly in the Southern Ocean where sloping density surfaces provide a direct pathway from the surface into the interior. While the qualitative nature of stirring seems clear, quantitatively characterizing properties of this stirring is necessary to build accurate parameterizations and understand how the ocean is ventilated. One way to characterize this is by quantifying the distribution of the tracer concentration as a function of scale. Here, we do this characterization by analyzing data collected by two gliders in a region where the mean current of the Southern Ocean meanders as it flows over topography, and is likely to be a hot spot for ventilation. This reveals that relatively small eddies generated by a process known as mixed layer instability are likely active in the mixed layer and play an important role in setting the near-surface stratification. Surprisingly, tracer structure below the mixed layer also indicates that flows with small horizontal and vertical scales play an important role in stirring. This challenges conventional wisdom, which assumes that only the largest eddies are important for stirring.

1 Introduction

Oceanic macroscale turbulence, encompassing flows at scales of 1-100 km, is efficient at stirring tracers and plays an important role in setting the transport and storage properties of climatically- and biogeochemically-relevant tracers. This stirring is particularly important in the Antarctic Circumpolar Current (ACC) of the Southern Ocean, where outcropping isopycnals provide an adiabatic pathway from the surface into the interior, and contributes to the Southern Ocean's disproportionately outsized impact in the evolution of the Earth's climate (Gille et al., 2022; Naveira Garabato et al., 2017).

Mesoscale turbulence ($\sim$ 100 km) is known to play a dominant role in setting stirring properties of the ACC, and this stirring is generally enhanced in regions downstream of topographic features (Thompson & Sallée, 2012; Roach et al., 2016; Tamsitt et al., 2017). These are also regions where a large part of the cross-ACC transport as well as exchange between the mixed layer and interior, which is required to ventilate the interior ocean and to close the meridional overturning circulation (MOC), takes place. These proper-

ties have been confirmed by observational studies, which have quantified the bulk properties of the stirring as eddy diffusivities, using both tracers (Tulloch et al., 2014) and floats (LaCasce et al., 2014; Balwada, Speer, et al., 2016; Roach et al., 2016). On the other end of the spectrum, microscale and finescale turbulence (< 100 m) erodes the along-isopycnal tracer variability that is cascaded down by mesoscale stirring. Garabato et al. (2016) showed that a sensitive link exists between this small-scale dissipation and the large-scale MOC, suggesting that it is vital to understand how tracer variance cascades from the mesoscale to the finescale.

Quantifying the details of stirring at the submesoscale $O(1 - 100$ km) helps address how and at what rates tracer filaments are drawn out by mesoscale eddies, broken down into smaller filaments, and eventually dissipated. In particular, the role of submesoscale processes needs to be quantified in order to develop a better understanding and theoretical models of this tracer cascade. Previous observational studies in the ACC have either suggested or assumed that tracer stirring is primarily non-local, as may be expected if the flow dynamics were akin to quasi-geostrophic (QG) dynamics (Polzin & Ferrari, 2004; Foussard et al., 2017). This assumption suggests that tracers are stirred predominantly by the mesoscale eddies and the smaller scale flows do not play an important role in the cascade of tracer variance. These ACC studies have quantified the details of the stirring using dispersion rates of tracer patches or float clusters, when these patches are smaller than the dominant eddies (van Sebille et al., 2015; Boland et al., 2015; Zika et al., 2020; Balwada et al., 2021).

An alternative way to characterize the nature of stirring is to quantify the distribution of tracer variance across spatial scales, as this tracer variance distribution is set directly by the characteristics of the tracer cascade if stirring is the dominant process. One method to quantify this scale-dependent distribution is to estimate the power law scaling of the tracer variance spectrum, and to quantify the resulting power law exponent, or "the slope of the spectrum." Theoretical investigation of tracer stirring predicts that the slope of the variance spectrum is inversely proportional to the slope of the kinetic energy (KE) spectrum; essentially, the higher the relative levels of KE at smaller scales, the more efficient the tracer cascade, and hence a smaller relative level of tracer variance at those scales (Vallis, 2017; K. Smith et al., 2002). For example, a steep KE spectrum of the form k^{-3}, produced in the enstrophy cascade in two-dimensional or QG turbulence, will result in a shallow tracer variance spectrum of the form k^{-1}, and is an example of non-local stirring. A shallower KE spectrum of the form $k^{-5/3}$, generated in the inverse-energy cascade in QG or by surface QG turbulence, will produce a relatively steep tracer variance spectrum of the form $k^{-5/3}$, and is an example of local stirring.

Recent observational studies, from the era of high-resolution observational sampling (Cole & Rudnick, 2012; Klymak et al., 2015; Callies & Ferrari, 2013; McCaffrey et al., 2015; Erickson et al., 2020; Jaeger, MacKinnon, et al., 2020), have shown that along-isopycnal tracer variance spectral slopes range between -1 and -2, with more studies estimating values closer to a steeper -2 slope. A review of these different observational studies by Jaeger, MacKinnon, et al. (2020) also suggests that in many regions the spectral slope is depth independent, but in a few regions it is found to become flatter near the surface. These studies have mostly analyzed observations from regions with relatively weak mesoscale eddy fields, and the spectral slopes suggest that stirring is more efficient at cascading tracer variance to small scales than predicted from conventional forced-dissipative QG turbulence.

The distribution of tracer variance across scales in regions with a more active mesoscale field, such as the ACC or western boundary currents, at scales smaller than 100 km and depths below the mixed layer, has not previously been investigated. Here, we analyze tracer observations collected by a pair of gliders deployed in an energetic region of the ACC during the Southern Ocean Glider Observations of the Submesoscales (SOGOS) experiment (Dove et al., 2021). The SOGOS gliders sampled a region downstream of the

Southwest Indian Ridge (SWIR), where the ACC meanders and sheds eddies as it flows over topography. The tracer structure revealed by these observations suggests that the mixed layer is replete with mixed layer eddies, likely produced by mixed layer instabilities, and that submesoscale flows in the interior play an important role in stirring tracers below the mixed layer.

We describe the glider datasets and the metrics used to characterize the scale-dependent statistical properties of the tracers in section 2. In section 3, we describe the climatological setting of the region and discuss how the dominant tracer anomalies in the glider sections are indicative of ventilation. The main results, the quantification of tracer structures using spectral and binning analysis, are presented in section 4. We then proceed to discuss how our results fit into the broader context in section 5, before summarizing and concluding in section 6.

2 Data and Methods

2.1 Glider observations and data

The SOGOS experiment was carried out in the Indo-Atlantic sector of the ACC during May - August 2019. The primary observations were carried out by a pair of Seagliders (SG659 and SG660) that followed a Biogeochemical-Argo float (Talley et al., 2019) and conducted high resolution sampling of the tracer field with the aim of estimating the variability that is aliased in the traditional ten-day Argo profiling period. A detailed summary of the observations and analysis showing that this region is a hot spot for ventilation was provided in Dove et al. (2021). In this study, we focus primarily on the glider observations at scales smaller than 100 km, which are unresolved by a single Argo float.

A summary of the glider observations is shown in Figure 1. The gliders covered a region of approximately 600 km by 400 km, and the individual gliders covered an along-track distance of approximately 1500 and 2200 km. The vertical sampling of the glider Conductivity, Temperature, and Depth (CTD) sensor has a median separation near 0.6 m, with the sampling distance rarely exceeding 1.5 m. Horizontally, the separation between dives varies depending on the depth, since the glider moves in a V-shaped pattern. Most of these separations are less than 4 km, and almost never exceed 7 km. Similarly, the temporal separation between the glider dives is between 4-6 hours, resulting in a 2-3 hour time separation at mid-depth. Details of the sampling resolution are shown in Figure S1, in the supplementary information (SI).

Conservative temperature and absolute salinity, referred to as temperature (T) and salinity (S) in the rest of this work, were estimated from the in-situ temperature and practical salinity measurements. Potential density referenced to the surface (σ), which will henceforth be referred to as density, was calculated from T and S. These thermodynamic variables were estimated using the TEOS-10 python toolbox (McDougall & Barker, 2011). The mixed layer depth (MLD) was estimated using a density criterion, where the mixed layer was defined as the depth where the density was higher than the 10 m density value by a value 0.03 kg m^{-3}. Spice anomaly ($d\tau$), used to quantify the thermohaline variations along isopycnals, was computed as $d\tau = 2\alpha dT$ (See SI section 1.3 for more details). Apparent Oxygen Utilization (AOU) is defined as $O_2^{sat} - O_2$ (Ito et al., 2004), where the saturation concentration of oxygen (O_2^{sat}) was also estimated using TEOS-10.

2.2 Spectral estimation

Power spectral density (PSD), of both density on constant depth surfaces and spice on constant density surfaces (isopycnals), provide insight into how tracer variability is partitioned across spatial and temporal scales. We use the multi-taper method (Prerau

et al., 2017) for spectral estimation, which is summarized in SI section 1.5. Variability of density at a constant depth is useful for analyzing the properties of the flow dynamics, such as mesoscale eddies, internal waves, and fronts. In contrast, the analysis of spice variability along isopycnals helps reveal how these flows stir tracers, since almost all of the tracer stirring occurs along isopycnals.

As the glider data is collected on a non-uniform grid (both spatially and temporally), it is not directly amenable to estimating Fourier transforms or spectral estimation, which require the data to be on a uniform grid. The observations are thus mapped onto a uniform grid using linear interpolation, where the grid resolution is chosen to be smaller than most of the smallest sampling separations, or 500 m in distance and 1 hour in time. This adjustment results in a steep roll-off in the power spectrum at the unresolved scales, due to the interpolation procedure. This roll-off starts to influence the wavenumber or frequency spectra at scales smaller than approximately 2-5 km or and 4-6 hours, respectively. This effect is seen in Figures 3 and 4, and so the corresponding scales are not visualized in Figure 8.

In the results below, we discuss both the frequency (ω) spectrum and the one-dimensional wavenumber (k) spectrum, computed along the glider trajectory. We also discuss two-dimensional spectra, in the frequency-vertical wavenumber ($\omega - k_z$) space and horizontal-vertical wavenumer ($k_x - k_z$) space. Each of these spectra provide a different vantage point in to the multi-scale structure of the variability observed by the gliders. However, since the glider is moving in space as it samples the region, the interpretation of these metrics is not as straightforward as their Eulerian counterparts, frequency spectra at a fixed point or wavenumber spectra at a fixed time snapshot.

When estimating the frequency spectra (Figure 3a), the complete time series of the glider data was used. The advantage of this approach is that it employs the full dataset, unlike when estimating the wavenumber spectra (discussed below), but the interpretation of some aspects is more challenging because the glider moved through the region relatively rapidly. The gliders were also advected by the current (tailwind current) or had the current advected relative to it (heading into the current), particularly during the first 20 days of the sampling. As a result, there is no obvious way to infer the underlying Eulerian frequency spectra. Even though the frequency spectra should not be precisely compared to any theoretical scalings, it can be used to interpret if the relative distribution of variance across time scales changes as a function of depth. This practice assumes that the aliasing and biasing that takes place due to motion of the glider relative to the measured field is similar through the upper 1000 m, which is a fair assumption for the relatively barotropic flow in the ACC.

The 1-D horizontal wavenumber spectra (Figure 3b and 4) are estimated only from the relatively straight sections collected by the gliders in the middle of the sampling campaign, around days 145 to 170 (Figure 1a). Additionally, for spice, this analysis is done along isopycnals (Figure 2b). The results are only presented for isopycnals that did not outcrop and were sampled over the entirety of the chosen section of the glider track. Over this period the gliders traversed approximately 420 km. The analysis in this study applies a frozen flow-field approximation. This is more appropriate at the higher wavenumbers or scales smaller than roughly 50-100 km, given that the glider traversed 15-25 km per day and flows at these spatial scales evolve on time scales of days to weeks.

When estimating the 2-D spectra of along isopycnal spice (Figure 8), the full dataset when one of the axes is frequency and only the relatively straight section when one of the axes is the horizontal wavenumber is used. For estimating properties along the other axis, the vertical wavenumber direction, the along isopycnal spice (Figure 2b) was mapped back to depth coordinates using the mean isopycnal depth (Figure 2c), and only mean isopycnal depth below the mixed layer, between 200-800 m, was used to estimate the spectra in the vertical wavenumber direction. Also, for this 2-D spectral estimation, a Han-

ning window with the xrft package was employed (`https://xrft.readthedocs.io/`), rather than the multi-taper approach.

2.3 Spatially binned statistics

An alternative method to quantify the variability as a function of scale is to consider the magnitude of tracer difference between two spatially-separated points, where the scale dependence is elucidated by considering different separation scales. For density or along isopycnal spice this amounts to considering the distributions of,

$$\triangle\phi(r) = \phi(\mathbf{x}+\mathbf{r},t) - \phi(\mathbf{x},t), \tag{1}$$

where $\phi(\mathbf{x},t)$ is the tracer concentration at location $\mathbf{x}$ and time t, and $\phi(\mathbf{x}+\mathbf{r},t)$ is the concentration at a second location that is separated by the position vector $\mathbf{r}$. In this study, all samples are averaged, and the spatial, temporal, or directional variability of these binned statistics are not considered. As a result, only the magnitude of the position vector $r = |\mathbf{r}|$ is considered and dependence of statistics on $\mathbf{x}$ and time t are dropped. This is roughly equivalent to assuming isotropy and homogeneity. Due to the natural stochasticity of the stirring processes that generate tracer variability, $\triangle\phi(r)$ is best viewed as a probability distribution function (PDF), and different statistical properties of this PDF provide information about the scale dependence of the variability.

Some of the relevant statistical properties of the $\triangle\phi(r)$ PDF can be quantified using structure functions. The n^{th} order structure function is defined as,

$$SF_n(r) = \langle \triangle\phi(r)^n \rangle\,, \tag{2}$$

where the $\langle . \rangle$ corresponds to an average over all available samples at a particular separation scale r. Here, the second, $SF_2(r)$, and normalized fourth order, $SF_4(r)/SF_2(r)^2$, structure functions, which describe the width and peakiness of the PDF, respectively, are described. These correspond to a measure of the variability and non-Gaussianity at different scales, respectively. Further, the $SF_2(r)$ is qualitatively a filtered version of the power spectrum – details of the exact analytical relationship can be found in Balwada, Speer, et al. (2016). For a large range of scales where the power spectrum follows a power law relationship ($k^{-(n+1)}$ for $1 < n < 3$), $SF_2(r)$ also follows a power law of the form $\sim r^n$. This implies that a $k^{-5/3}$ power spectrum corresponds to $\sim r^{2/3}$ structure function relationship, and k^{-3} corresponds to $\sim r^2$. However, a specific separation scale (r) should not be compared to a specific wavelength ($1/k$), as the real space and spectral space metrics do not have a precise scale to scale mapping and are only related through integral relationships (Davidson, 2015).

Binned statistical measures are more amenable to non-uniform sampling and also allow consideration of tracer variability at slightly smaller scales than the spectral analysis, as the information at these smallest scales does not get smoothed out during the gridding procedure needed for spectral estimation. If there are many observational platforms in the water at close range, then the pairings required to compute the differences can be done using only simultaneous measurements (Balwada, LaCasce, & Speer, 2016; Erickson et al., 2020; Callies et al., 2020; Balwada et al., 2022). However, when only one or two instruments are present, as is the case in this study, it is necessary to include samples that are also separated in time to augment the number of samples. This is equivalent to making a frozen field approximation, but with control over the maximum temporal separations that are permitted at any particular separation scale. Since structures at smaller scales evolve more rapidly than the structures at larger scales, $dT \leq 0.002r^{2/3}$ was empirically chosen, where dT is the time separation between two samples (distribution of pairs is shown in Figure S7). This form was roughly motivated based on the idea that turbulent eddy turnover time (T_{eddy}) scales like $T_{eddy} \sim (E(k)k^3)^{-1/2}$ and the assumption that $E(k) \sim k^{-5/3}$. The results presented below, PDFs and structure

functions for the mixed layer density and along-isopycnal spice, are not sensitive to this choice.

Density anomalies can have contributions from both T and S variations, which can be expressed as $\triangle\sigma(r) = \sigma_0 g(\alpha\triangle T(r) - \beta\triangle S(r))$. Here g is the gravitational acceleration, σ_0 is a reference density, and α and β are the thermal and haline expansion coefficients computed for each sample. The relative contributions of T and S variations on density variations can be quantified by the Turner angle (Ferrari & Rudnick, 2000; Giddy et al., 2021),

$$Tu(r) = \tan^{-1}(\frac{\alpha\triangle T(r)}{\beta\triangle S(r)}), \tag{3}$$

where considering samples at different separations (r) allows us to quantify the scale dependence of this metric. The Turner angle (Tu) varies between $\pm\frac{\pi}{2}$. $Tu > 0$ corresponds to cases where the T and S gradients cancel or compensate each others' influence on the buoyancy gradients, and $Tu < 0$ corresponds to the cases where T and S gradients act together to enhance the buoyancy gradient. $Tu = \frac{\pi}{4}$ corresponds to a perfect compensation between T and S, such that there are gradients in T and S but no corresponding buoyancy gradients. $Tu = -\frac{\pi}{4}$ corresponds to the case where the the T and S gradients are aligned and contribute equally to the buoyancy gradient. Salinity contributions dominate where $|Tu| < \frac{\pi}{4}$ and temperature contributions dominate when $|Tu| > \frac{\pi}{4}$.

2.4 Characterizing the 3D structure of tracer filaments

The metrics considered above, with the exception of 2-D spectra, characterize the structure of tracers along a single dimension, either at fixed depth or along particular isopycnals. However, oceanic stirring is a three-dimensional process that is driven by both shear and strain, which is capable of drawing out complex 3-D tracer filaments even if the flow is adiabatic (e.g. K. S. Smith & Ferrari, 2009). Here, we describe a couple of ways to investigate the cross-isopycnal coherence of these 3-D filaments, which are only sampled along 2-D sections by the gliders.

2.4.1 Visualizing layering

Stirring can generate layering in the interior ocean by intermingling disparate water masses. We use the diapycnal spice curvature (DSC) (Shcherbina et al., 2009) to visually highlight layering in our glider sections. DSC is defined as

$$\tau_{\sigma\sigma} \approx 2\alpha\sigma T_{\sigma\sigma} \approx 2\beta\sigma S_{\sigma\sigma}, \tag{4}$$

and is a visual indicator of water mass interleaving. Since the DSC is the second derivative, it is a noisy quantity and requires smoothing of the tracer fields before it can be computed. Details of the smoothing procedure are provided in the SI section 1.3.

In the absence of lateral advection, diapycnal mixing reduces and eventually destroys the curvature of the vertical tracer profiles, as the DSC appears in the term corresponding to diapycnal diffusion in the spice equation (equation 4 in Shcherbina et al., 2009). Conversely, high $|\tau_{\sigma\sigma}|$ indicates a sharp interface between dissimilar water masses, often a result of ongoing or recent differential lateral advection.

2.4.2 Tracer aspect ratio

The aspect ratio of tracer structures, spice (τ) structures in our observations, can be measured using the ratio of the vertical and horizontal gradients, $\alpha = L/H \sim |\tau_z|/|\tau_x|$, which quantifies the slope of tracer structures. This ratio is set by the relative strength of the vertical shear, which tilts tracer filaments and enhances vertical gradients, to strain, which enhances horizontal gradients (see appendix B in K. S. Smith & Ferrari, 2009).

K. S. Smith and Ferrari (2009) showed that in QG simulations, this aspect ratio is approximately N/f, where N is the buoyancy frequency and f is the Coriolis frequency, as that is the strength of shear to strain.

3 Overview of the region, glider sections, and ventilation signatures

The two SOGOS gliders sampled a sector of the ACC to the east of the Southwest Indian Ridge (SWIR), between $30-40^o$E and $50-54^o$S (Figure 1a, e). This region is just to the south of the climatological Polar Front location, which is defined as the northern most extent of the cold winter water at approximately 200m depth (Figure 1d). This is also a region where the ocean transitions from an α ocean, where density is controlled by T, to a β ocean, where density is controlled by S (Stewart & Haine, 2016), and most of the water masses sampled by the gliders seem to be from the β regime (Figure 1d). The T sections look visually very similar to spice due to this predominant sampling of the β regime (compare Figure 2a or b to 2c). A more detailed examination of the hydrography, and the association between cold T anomalies and ventilation to south of the PF appears in Dove et al. (2021).

As the ACC flows over the SWIR, it is topographically guided northward, which results in a northward excursion of the associated tracer contours (Figure 1e) and heightened mesoscale variability downstream of the ridge (Figure 1a in this study or Figure 2a in Dove et al. (2021)). Signatures of this enhanced mesoscale variability are clearly visible in the glider sections (Figure 2a); the isopycnals heave ∼100-300 m as the gliders navigate through the mesoscale eddies. The isopycnals also show finer scale heaving, ∼10-50 m, due to a rich internal wave and tidal field. The associated T and spice sections also show a complex structure, with prominent temperature anomalies relative to the climatological mean, O(0.5^o C). These anomalies are skewed towards anomalously colder T (Figure 1e inset), suggesting their origin to be in the cold winter waters. Visually, these large anomalies appear to be associated with the mesoscales, spanning lateral scales of $100-200$ km and vertical scales of $100-500$ m, and extending to depths from the mixed layer base up to roughly 700 m (e.g. Figure 1b, c, e). Additionally, these anomalies are strongest in the first part of the glider section (year day 120-150), when the gliders were sampling a region that had stronger mesoscale eddies.

Sections of tracers show intricate structure at many scales, in addition to the largest tracer anomalies (Figure 2). The anomalies spanning across large depth ranges are likely formed due to lateral stirring by the barotropic flow, and evidence of the baroclinic vertical shear impacting tracer structures can be seen in the layered structures of the anomalies. This can be seen most clearly seen when visualizing water mass layering through DSC (Figure 2d). The DSC shows the presence of layered features, with characteristic thickness of $O(50$ m) and horizontal coherence that often spans $O(100$ km), throughout the entirety of the glider sections. Usually the layers associated with colder waters have a larger magnitude of DSC (e.g. between 220-400 km) while the warmer waters have smaller magnitude of DSC and slightly flatter layers, suggesting that the layers in colder waters are more recently subducted than the layers in the water waters. This might be the case if the colder waters were recently subducted to depth while the warmer waters are associated with the much older Circumpolar Deep Water (CDW) mass. It is also worth noting that these waters with variable ventilation signatures are present on the same isopycnals and can be stirred together adiabatically.

The layering provides evidence of the 3-D nature of tracer stirring in the ocean, suggesting it is likely to play an important role in the cascade of variance to small scales and its ultimate dissipation by vertical diffusion. K. S. Smith and Ferrari (2009) showed that such intricate tracer patterns and layering can develop even in idealized QG models due to the combined effect of horizontal strain and vertical shear on tracer gradients, and both the strain and shear can play an important role in the tracer variance cascade. Similar

structures that span isopycnals have also been observed at other locations, (e.g. Jaeger, MacKinnon, et al., 2020; Shcherbina et al., 2009), but these observations are some of the first ones in a region with a highly active mesoscale eddy field. In the next section the details of this tracer variance cascade are quantified by estimating the statistical distribution of the tracer variance as a function of length and time scales. This cascade eventually leads to dissipation and irreversible mixing, which is essential for permanently subducting and sequestering tracers from the surface to the interior (Garabato et al., 2016).

4 Statistical description of tracer structures

Complementary to the identification of coherent mesoscale (eddy) and submesoscale (filamentary) structures in the glider data, presented in the previous section and in Dove et al. (2021), here an assessment of the statistical properties of the tracer distribution reflecting stirring processes in this region is presented.

4.1 Spectral Analysis

4.1.1 Density spectra at fixed depth

The frequency spectra (Figure 3a, also see Figure S5) show that density variance at all depths generally decreases as frequency increases. In addition to this decrease, isolated peaks corresponding to the inertial frequency and semi-diurnal tide clearly stand out in the interior (dashed white lines in Figure 3a), and their energy content decreases away from the mixed layer. The density variance at the largest scales generally decays deeper in the water column, except for a marked reduction in large scale density variance near the base of the mixed layer where the stratification is the strongest.

The wavenumber spectra (Figure 3b, also see Figure S5) also show a strong depth dependence, as in the frequency spectra. Similar to the frequency spectra, the large scale variance peaks in the mixed layer and in the thermocline, with a notable minima at the base of the mixed layer. There is also a reduction in variance at small scales in the middle of the mixed layer, relative to the surface and mixed layer base. However, unlike the frequency spectra, there are no isolated peaks corresponding to the near-inertial waves of tides in the interior; these phenomena generally have a broad band signature in wavenumber.

One of the striking features of the density spectra is that the rate of attenuation of density variance with increasing frequency or wavenumber changes non-monotonically with depth. The attenuation rate is quantified by fitting a power-law, ω^p, to the spectrum in a range of frequencies that correspond to time period of 18 hours to 10 days (sub-inertial frequencies) at each depth. This range was chosen to span the range between the largest resolved scales, which depends on the window size choices made in the multi-taper method, and the smallest scales where the influence of the waves starts to become important. Similarly, a power law is fit to the wavenumber spectra, k^q, over a wavenumber range corresponding to length scales of 5-50 km, where the range is chosen to avoid the scales where the variance decays due to the linear interpolation used in the horizontal gridding. The spectral slopes p and q are shown in the figures alongside the main panels in Figure 3.

Both the wavenumber and frequency spectral slopes are shallow, around -2, near the surface, get steeper, around -3, in the middle of the mixed layer, and then get shallower again near the base of the mixed layer. The enhanced small-scale variance at the surface and at base of the mixed layer, where N^2 is large, is likely indicative of frontal formation in these regions. This result hints at dynamical processes that are similar to mixed layer instability (MLI; discussed further in section 5.2). MLI results in a density wavenumber spectra with a slope of $-5/3$ at the surface and mixed layer base that gets

steeper in the middle of the mixed layer, as can be seen from the spectra of potential energy in a QG model of MLI in Figure 14 of Callies et al. (2016). In contrast, the spectral slopes in the interior are distinct for the frequency and wavenumber spectra, -3 and -2 respectively, and these wavenumber spectra agree roughly with the empirical scaling of internal wave spectrum from Garrett-Munk model (Garrett & Munk, 1975).

4.1.2 Spice spectra along isopycnals

The ocean interior is predominantly adiabatic, and the isopycnal heaving, as shown above, is dominated by internal waves. To characterize the tracer structures generated by stirring along isopycnals, we estimate wavenumber spectra of spice in isopycnal coordinates and fit a power law of the form k^q to the spectral estimate between scales of 5-50 km.

The spectral slopes of spice on all density surfaces are steeper than would be predicted based on non-local stirring, such as the enstrophy cascade range of the quasi-geostrophic model (K. Smith et al., 2002; K. S. Smith & Ferrari, 2009). The wavenumber spectra of spice (Figure 4) show that there is some variation in spice variance across isopycnals, with the greatest amount of large-scale spice variance present on isopycnals 27.2-27.5 kg m^{-3}, located a few hundred meters below the base of the mixed layer. The spectral slope is approximately -2 over the majority of the isopycnals (Figure 4 side panel, and Figure S6). This spectral slope is indicative of frontal features in the tracer fields, likely formed by the ventilated filaments. The slopes for some of the deeper sampled isopycnals (σ between 27.5 - 27.6 kg m^{-3}, and mean isopycnal depth roughly between 500-700 m) are even steeper, around -3. These isopycnals also have a marked reduction in large-scale along isopycnal variance and are below isopycnals where the prominent subduction anomalies are present (Figure 2c,d). As a result, these steeper slopes are likely a result of weak large scale tracer gradients (Figure 1d,e) resulting in a smooth tracer field.

4.2 Binned Statistics: Gradient PDFs and Structure Functions

Complementary to the spectral analysis presented above, here the binned statistics of vertically averaged density in the mixed layer and spice along isopycnals are presented. As described in section 2.3, one significant advantage of using this metric, rather than the 1-D wavenumber spectrum, is that data on straight lines and uniform grids are not necessary.

4.2.1 Binned statistics in the mixed layer

In the mixed layer, the observed density gradient PDF at each scale roughly resembles a negatively skewed log-normal distribution that spans about 2-3 orders of magnitude (Figure 5a), implying that the mixed layer is replete with a few sharp fronts interspersed with large regions of weak gradients. These density gradient PDFs migrate to larger magnitudes as the length scales gets smaller, suggesting that density fronts are amplified at smaller scales. The mean of this density gradient PDF approximately follows a power law with slope of $-3/5$, indicating an increase in the mean strength of the density gradients by about 15 times from scales of 100 km to 1 km. This power law behavior is akin to a spectral slope of the density power spectrum of around -1.8, between -2 and -5/3, complementing the spectral estimates that were described earlier in section 4.1.1. At scales smaller than roughly 500 m, the magnitude of the density gradients saturates, which might indicate that density fronts have reached a balanced state. However, this may not be a robust signal due to the limited sampling and sensitivity to the data processing algorithm at these scales.

The observed density gradients are a result of a combination of gradients of temperature and salinity, and the relative strength of the two contributions is quantified us-

ing the Turner angle. The PDF of the horizontal Turner angle in the mixed layer (Figure 5b) peaks around a value of $-\frac{\pi}{4}$ at scales between 500 m-100 km, and this peak transitions to a value between $-\frac{\pi}{4}$ to 0 at smaller scales. This indicates that over most of the scales the temperature and salinity gradients are aligned and contribute equally towards the density gradient, while at the smallest scales this balance shifts towards salinity gradients starting to play a more important role in setting the strength of the density fronts. However, the signal at scales smaller than 500 m might be impacted by the limited sampling and data processing steps (e.g. thermal lag correction between up and down dives), and should be interpreted with caution.

4.2.2 Binned statistics along isopycnals

The intensification of along-isopycnal spice gradients at smaller scales is also apparent in the ocean interior, shown by PDFs of spatial gradients as a function of horizontal scale (Figure 6a). The shape of this PDF and its dependence on scale is also similar to the density gradient PDF in the mixed layer, with a slightly narrower range of possible magnitudes at each scale. For ease of comparison between different isopycnals and comparison to theoretical scalings, the properties of these distributions are quantified using the 2^{nd} and normalized 4^{th} order structure functions, SF2 and SF4 respectively.

SF2 increases as a function of separation scale and has a tendency to saturate at scales larger than approximately 10-20 km (Figure 6b or S7), suggesting that the spice signals become de-correlated at this scale. The maximum value of SF2, a measure of the total spice variance, peaks on isopycnals between 27.3-27.5 kg m^{-3}, similar to the spectral estimates presented in section 4.1.2. Corresponding to this greater large-scale SF2, the magnitude of SF2 at smaller scales is also enhanced on these isopycnals. Note that this is in slight contrast to the spectral estimate (Figure 4), which had a relatively more uniform level of smaller scale variance at the higher wavenumbers. A power law fit to SF2 (r^s), which suggests a SF2 slope between $2/3 \sim 1$ (Figure 6b side panel or Figure S7) and equivalent to a spectral slope between $-5/3 \sim -2$, is in rough agreement with the spectral estimates. The slight discrepancy between the SF2 and the wavenumber spectra can be a result of the structure functions being a less scale selective metric or a result of the SF2 being computed over the full glider deployment while the wavenumber spectra were over only the straight sections.

The SF4s generally have small values at larger scales (10-100 km), and increase at smaller scales, implying that the spice gradient distributions are more Gaussian-like at larger scales and systematically develop longer tails at smaller scales (Figure 6c). Therefore, at smaller scales, there is a higher probability of encountering strong fronts separated by patches of relatively homogeneous spice, consistent with the analysis of spice in the North Pacific (Klymak et al., 2015).

4.3 2-D Characterization of tracer structures

Tracer stirring is a 3-D process and generates coherent structures that have an imprint in the horizontal and vertical directions, as evidenced by spice structures that show coherence in depth and along the glider sections (e.g. Figure 2). Considering that the cross-isopycnal flow in the ocean is relatively weak, these structures emerge because the along-isopycnal flow at different depths is correlated. As horizontal strain draws out filaments, they tilt as a result of the vertical shear. Here we use some of the same metrics as K. S. Smith and Ferrari (2009) to quantify the properties of the tracer filaments and compare the results to predictions from QG theory.

Quantification of the 2-D properties of spice anomalies can be achieved via the aspect ratio, defined as the ratio of their horizontal and vertical scales, and estimated by

the ratio of horizontal and vertical spice gradients, τ_x and τ_z, respectively. While there is a large degree of variability in the aspect ratio (Figure 7a), the average value is $O(100)$ (Figure 7b), with values of approximately 200 just below the mixed layer that decrease to a relatively uniform value of 80-90 in the interior. QG theory predicts the aspect ratio to be N/f, which varies between 20-40; the observed aspect ratio is approximately 4-5 times greater in the interior. The relatively large measured aspect ratio implies that tracer filaments in this region are flatter, meaning the filaments are more stretched out horizontally or more narrowed vertically. As a result, the ratio of the vertical shear experienced by the filaments to the horizontal strain they encounter is larger than would be expected according to QG theory (discussed further in section 5.3).

An alternative approach to quantifying the 2-D tracer distribution is to estimate the 2-D tracer spectra computed in vertical-wavenumber and either horizontal-wavenumber or frequency space (Figure 8). The 2-D spectra show that tracer variance is greatest at the largest scales and decreases at smaller scales, both in the horizontal and vertical directions. While the limits of the glider dataset result in a relatively noisy estimate, the peak in spice variance clearly extends in the horizontal-vertical wavenumber space along the line of the observed aspect ratio, rather than along N/f (compare the dashed black and gray lines in Figure 8b). Integrating these 2-D spectra along the vertical-wavenumber axis gives the vertically-averaged along-isopycnal spectra as a function of frequency or horizontal-wavenumber (Figure 8 d,e), as discussed in section 4.1.2. Integrating along the horizontal-wavenumber or frequency axis returns a 1-D spectrum as a function of vertical-wavenumber (Figure 8c). This 1-D spectrum shows an interesting signal, with a flatter -2 spectral slope at scales larger than 100 m and a steeper -3 slope at scales smaller than 100 m, suggesting a more rapid rate of variance decay (i.e., a smoother tracer field) at scales less than 100 m.

5 Discussion

The data collected by the SOGOS gliders allowed for a novel exploration of the tracer structures and their scale dependence near the core of the ACC. The standing meander near the SWIR is a region where cold, fresh waters from the south of the PF are subducted and then stirred with older interior water masses. In the interior, stirring cascades this tracer variance to small scales in the horizontal (along isopycnals) and in the vertical due to the combined action of along-isopycnal stirring and vertical shear. The rate of this cascade is more efficient than what is expected from non-local stirring, implicating the importance of submesoscale flows in the stirring process throughout the water column. In the mixed layer, stirring cascades density variance to smaller scales, forming fronts, and is particularly active near the surface and base of the mixed layer, suggesting that a mechanism similar to MLI is likely resulting in boundary layer restratification.

5.1 Origin of larger scale tracer filaments

The mean eastward flow of the ACC and the associated isopycnal shoaling along the poleward side of the PF, combined with high mesoscale eddy variability and northward excursion of mean tracer contours (Figure 1d,e), makes this region kinematically susceptible to subduction. Mesoscale meanders and eddies can draw out cold surface waters from south of the Polar Front and propel them in filaments across the southward excursion of the mean geostrophic stream lines of the ACC, further aided by the slow eastward drift of the eddies. Such ventilation pathways are seen in high resolution numerical simulations, e.g. see Figure 5 in Morrison et al. (2022). The glider sections show examples of deep reaching cold filaments, potentially sourced from the winter water south of the PF, (e.g. at horizontal distance 220-400 km and 450-650 km in Figure 2a,b), which are also associated with lower AOU concentrations, indicating more recent contact with

the surface (Figure 2d). A more in-depth study of these filaments, their link to subduction and ventilation, the role of mesoscale versus submesoscale flows, and their regional variation can be found in Dove et al. (2021) and Dove et al. (2022). In this study, we focus on understanding how these large filaments and tracer gradients are stirred and cascaded to smaller scales, where they can be irreversibly dissipated.

5.2 Tracer variability in the mixed layer

Dove et al. (2021) showed that during the SOGOS experiment, the mixed layer depth was highly variable, with a mean mixed layer depth of approximately 120 m and standard deviation of 35 m, and greater variability in regions of high strain and kinetic energy. The scale-dependent analysis of thermohaline and density structures in this study shows that, compared to the interior, the mixed layer develops relatively strong small-scale density gradients. Furthermore, these density gradients are enhanced near the surface and the base of the mixed layer (Figure 3), and are formed by roughly equal contribution from T and S gradients at scales between 500 m and 100 km (Figure 5).

The vertical structure of the mixed layer density spectra, particularly the enhanced small-scale variance at the surface and base of the mixed layer (Figure 3), is reminiscent of the idealized QG description of MLI and its non-linear equilibration presented by Callies et al. (2016). This structure likely results from the boundary dynamics, where a reduction of vertical velocity at the surface boundary and regions with sharp stratification changes allows density variance to cascade to small scales. The smaller-scale modes decay away more rapidly from the boundary than the larger scales, resulting in the depletion of small-scale variance in the middle of the mixed layer.

Taking this vertical structure as evidence that the lateral boundary layer dynamics are akin to MLI, a speculative dynamical description of boundary layer dynamics can be inferred. The dynamics of MLI involves a downscale cascade of potential energy to the ML deformation radius, a conversion to KE, which then cascades to larger scales in an inverse cascade. While the dynamics in the real ocean are more intricate than a QG model description, MLI likely plays an important role in the restratification of the mixed layer by releasing available potential energy. Some observational confirmation of the first order importance of MLI in the evolution of the mixed layer depth was presented in Du Plessis et al. (2019), and modeling evidence of its importance in high resolution simulations was presented by Su et al. (2018).

Mixed layer density fronts, across scales from 500 m to 100 km, are formed by equal contributions from T and S gradients, and do not indicate much compensation. This might be in part because this data is from a region where the ocean density transitions from being dominated by T to being dominated by S, or from an α to a β ocean (Stewart & Haine, 2016). This is in contrast to observations of mid-latitude mixed layers, in an α ocean, showing an abundance of compensated thermohaline fronts (Rudnick & Ferrari, 1999; Ferrari & Rudnick, 2000; Rudnick & Martin, 2002; Hosegood et al., 2006), which have no associated density fronts. These compensated fronts are hypothesized to form when frontogenetic process, i.e., eddy straining and/or laterally variable surface fluxes, are relatively weak or intermittent. Under these conditions, the density fronts relax, while compensated fronts persist for much longer. The lack of compensation in the SOGOS region suggests that most of the density fronts here result from strong, prolonged lateral stirring, a consequence of the vigorous eddy field, while sporadic atmospheric forcing contributes much more weakly to the generation of fronts. A lack of thermohaline compensation has also been observed in other regions. For instance, density gradients in the Arctic Ocean and in regions to the south of the PF in the Southern Ocean form primarily due to salinity gradients (Timmermans & Winsor, 2013; Giddy et al., 2021), while the region near the North Pacific Subtropical Front around 28°N is seen to primarily form density fronts due to temperature gradients (Hosegood et al., 2006). How-

ever, the lack of compensation found in those areas may be due to weak large-scale variation of the alternative thermodynamic tracer, which stands in marked contrast to the PF region of the ACC studied here.

5.3 Tracer variability in the interior

The horizontal structure of density and tracers in the interior ocean has small-scale variance as a result of lateral stirring and internal wave heaving, a significant part of which comes from near-inertial waves and semi-diurnal tides (Figure 3). The scale dependence of spice along isopycnal surfaces was analyzed to remove the heaving signal and thus isolate the structure that is created by along-isopycnal stirring.

The scale dependence of along-isopycnal spice variance, as estimated from both the spectra and structure functions, shows that the tracer variance decays more rapidly with length scale than would be expected based on non-local stirring (Figures 4, 6). This result is similar to observational estimates of the spice spectra from other regions, including the North Pacific, North Atlantic, and the Bay of Bengal (Cole & Rudnick, 2012; Callies & Ferrari, 2013; Klymak et al., 2015; Erickson et al., 2020). However, this finding based on spice spectra contrasts the suggestion of non-local stirring put forth in recent studies based on analysis of dispersion statistics from deep neutrally-buoyant, acoustically-tracked float trajectories (Ollitrault et al., 2005; Balwada et al., 2021; Rossby et al., 2021). This distinction could be due to differences in the sensitivity of the metrics used for this characterization or could be caused by the limited spatial sampling resolution of such floats, which typically can not resolve separation scales smaller than ∼1-3 km. This can be contrasted with separation scales of ∼10 km, where the SF2 of along-isopycnal spice starts to saturate in Figure S7.

A number of different mechanisms can generate the observed rapid decay of spice variance in wavenumber space. Mechanisms based on inertial theories like the inverse energy cascade initiated by patches of breaking internal waves (Polzin & Ferrari, 2004) or stratified turbulence (Brethouwer & Lindborg, 2008) would suggest a power law scaling of $k^{-5/3}$. The presence of fronts in spice along isopycnals, regardless of the dynamics, would suggest a power law scaling of k^{-2}. Interaction between internal waves and balanced eddies can also generate small scale features in the balanced flows, which could increase the efficiency of the variance cascade and result in steeper spectra (Thomas & Yamada, 2019). Future work is needed to distinguish and identify which (if any) of these mechanisms is the dominant source the observed spice variance.

The observed tracer structures are three dimensional, span many isopycnals, and are often vertically tilted, suggesting that the tracer variance simultaneously cascades to smaller scales in the horizontal and vertical. Theoretical investigation of 3-D cascades has been done using idealized QG models (K. S. Smith & Ferrari, 2009; Haynes & Anglade, 1997; Charney, 1971), where vertical shear tilts the horizontal tracer filaments to generate finer vertical-scale structures thereby resulting in a tracer aspect ratio (the ratio of the horizontal and vertical scales of tracer structures) of N/f. However, the aspect ratios of tracer structures calculated in this region, around 100, were much flatter than what QG theory would suggest ($N/f \sim 20$) and were elevated close to the base of the mixed layer. Previous observational studies have shown that tracer structures in other parts of the ocean are also flatter than predicted by QG theory (Jaeger, Lucas, & Mahadevan, 2020; Cole & Rudnick, 2012; Pietri et al., 2013). Additionally, high-resolution numerical simulations (Siegelman, 2020) and flow observations (Yu et al., 2019; Siegelman et al., 2020) have suggested departure from QG dynamics or low Rossby number flows, in regions below the mixed layer. One interpretation of the observations of flatter tracer filaments is that the Burger number (Bu) in this case is larger than O(1), in disagreement with the assumption of O(1) Bu usually made in QG theory. Alternatively, it is possible that the Bu for the overall flow is O(1), but that the observed filaments per-

sist as coherent features for longer than the filaments that form in QG theory, allowing for vertical shear to tilt them for a significantly longer duration. This hypothesis would be consistent with the result shown in section 4.1.2 that the horizontal spice distribution is dominated by fronts, which also do not form in QG models.

Finally, the tracer structures at vertical scales smaller than 100 m are smoother than those predicted by QG theory (Figure 8c). This smoothing may be indicative of the scales where the 3-D tracer variance cascade starts to experience dissipation and where shear dispersion results in rapid diffusion of tracer variance.

6 Summary and Conclusions

The SOGOS glider campaign provides a unique view of the tracer structures that form downstream of the Southwest Indian Ridge, where the standing meander formed by the interaction between the Polar Front and the topography becomes unstable and meanders. This region is highly energetic, making it distinct from other regions where small-scale tracer structure has been analyzed previously. The glider sections captured instances of tracer filaments, composed of cold winter water from south of the PF, that are being subducted along the fast-moving meander. As described in Dove et al. (2021), once water is subducted it is rapidly stirred by energetic ACC eddies, and the resulting tracer gradients are cascaded to smaller scales. Here, we study this cascade process by analyzing the scale-dependent distribution of tracer variance that emerges. This cascade feeds variance to the irreversible mixing that occurs at the smallest scales and is thus an essential step in the long-term storage of subducted tracers in the interior ocean.

The density variability in the mixed layer shows a marked increase in small scale structures, likely fronts, near the surface and at the base of the mixed layer. This is suggestive of active surface QG dynamics at the boundary and at depths with sharp stratification changes. These results thus provide novel observational evidence that mixed layer instabilities likely fuel the non-linear dynamics of the small-scale flows in the upper ocean, thereby playing an active role in restratification (Boccaletti et al., 2007; Callies et al., 2016) and the heat budget of the mixed layer (Su et al., 2018).

The scale-dependent distribution of along-isopycnal tracer variance shows that there is less tracer variance at smaller scales than would be expected based on non-local stirring, as exemplified by the enstrophy cascade of QG dynamics. This result suggests that the tracer variance is transferred to smaller scales more rapidly than in an enstrophy cascade, hinting that the presence of submesoscale flows in the interior ocean plays an active role in tracer stirring (Siegelman et al., 2020; Yu et al., 2019). The exact dynamics of these flows, whether they are balanced or wave-like, can not be constrained from the dataset that is the subject of this study and necessitate further investigation. In addition, the novel observational results presented here have potential implications for the design of parameterizations in intermediate resolution simulations that only partially resolve mesoscale eddies.

Acknowledgments

The SOGOS data analyzed in this study and the code to do the analysis and produce the figures can be found on `https://github.com/dhruvbalwada/SWIR_ACC_glider_tracer_analysis`. The glider data are also archived at NOAA's National Centers for Environmental information and can be accessed at `https://www.ncei.noaa.gov/archive/accession/0228185` and `https://www.ncei.noaa.gov/archive/accession/0228187`.

This work was supported by NSF awards OCE-1756956 and OCE-1756882. ARG received additional support from NASA through award NNX80NSSC19K1252, from the U.S. Argo Program through NOAA award NA20OAR4320271, and from NSF's Southern Ocean Carbon and Climate Observations and Modeling (SOCCOM) project through

award OPP-1936222. LAD and AFT were supported by NSF award OCE-1756956, the David and Lucille Packard Foundation, and the Resnick Sustainability Institute. LAD was additionally supported by an NSF Graduate Research Fellowship. The authors are also extremely grateful to Geoff Shilling and Craig Lee for their time and effort in re-processing the glider data using the latest processing routines.

References

Balwada, D., LaCasce, J. H., & Speer, K. G. (2016). Scale-dependent distribution of kinetic energy from surface drifters in the gulf of mexico. *Geophysical Research Letters*, *43*(20), 10–856.

Balwada, D., LaCasce, J. H., Speer, K. G., & Ferrari, R. (2021). Relative dispersion in the antarctic circumpolar current. *Journal of Physical Oceanography*, *51*(2), 553–574.

Balwada, D., Speer, K. G., LaCasce, J. H., Owens, W. B., Marshall, J., & Ferrari, R. (2016). Circulation and stirring in the southeast pacific ocean and the scotia sea sectors of the antarctic circumpolar current. *Journal of Physical Oceanography*, *46*(7), 2005–2027.

Balwada, D., Xie, J.-H., Marino, R., & Feraco, F. (2022). Direct observational evidence of an oceanic dual kinetic energy cascade and its seasonality. *Science Advances*, *8*(41), eabq2566.

Boccaletti, G., Ferrari, R., & Fox-Kemper, B. (2007). Mixed layer instabilities and restratification. *Journal of Physical Oceanography*, *37*(9), 2228–2250.

Boland, E. J., Shuckburgh, E., Haynes, P. H., Ledwell, J. R., Messias, M.-J., & Watson, A. J. (2015). Estimating a submesoscale diffusivity using a roughness measure applied to a tracer release experiment in the southern ocean. *Journal of Physical Oceanography*, *45*(6), 1610–1631.

Brethouwer, G., & Lindborg, E. (2008). Passive scalars in stratified turbulence. *Geophysical research letters*, *35*(6).

Callies, J., Barkan, R., & Garabato, A. N. (2020). Time scales of submesoscale flow inferred from a mooring array. *Journal of Physical Oceanography*, *50*(4), 1065–1086.

Callies, J., & Ferrari, R. (2013). Interpreting energy and tracer spectra of upper-ocean turbulence in the submesoscale range (1–200 km). *Journal of Physical Oceanography*, *43*(11), 2456–2474.

Callies, J., Flierl, G., Ferrari, R., & Fox-Kemper, B. (2016). The role of mixed-layer instabilities in submesoscale turbulence. *Journal of Fluid Mechanics*, *788*, 5–41.

Charney, J. G. (1971). Geostrophic turbulence. *Journal of the Atmospheric Sciences*, *28*(6), 1087–1095.

Cole, S. T., & Rudnick, D. L. (2012). The spatial distribution and annual cycle of upper ocean thermohaline structure. *Journal of Geophysical Research: Oceans*, *117*(C2).

Davidson, P. A. (2015). *Turbulence: an introduction for scientists and engineers*. Oxford university press.

Dove, L. A., Balwada, D., Thompson, A. F., & Gray, A. R. (2022). Enhanced ventilation in energetic regions of the antarctic circumpolar current. *Geophysical Research Letters*, *49*(13), e2021GL097574.

Dove, L. A., Thompson, A. F., Balwada, D., & Gray, A. R. (2021). Observational evidence of ventilation hotspots in the southern ocean. *Journal of Geophysical Research: Oceans*, *126*(7), e2021JC017178.

Du Plessis, M., Swart, S., Ansorge, I. J., Mahadevan, A., & Thompson, A. F. (2019). Southern ocean seasonal restratification delayed by submesoscale wind–front interactions. *Journal of Physical Oceanography*, *49*(4), 1035–1053.

Erickson, Z. K., Thompson, A. F., Callies, J., Yu, X., Garabato, A. N., & Klein, P. (2020). The vertical structure of open-ocean submesoscale variability during a full seasonal cycle. *Journal of Physical Oceanography*, *50*(1), 145–160.

Ferrari, R., & Rudnick, D. L. (2000). Thermohaline variability in the upper ocean. *Journal of Geophysical Research: Oceans*, *105*(C7), 16857–16883.

Foussard, A., Berti, S., Perrot, X., & Lapeyre, G. (2017). Relative dispersion in generalized two-dimensional turbulence. *Journal of Fluid Mechanics*, *821*, 358–383.

Garabato, A. C. N., Polzin, K. L., Ferrari, R., Zika, J. D., & Forryan, A. (2016). A microscale view of mixing and overturning across the antarctic circumpolar current. *Journal of Physical Oceanography*, *46*(1), 233–254.

Garrett, C., & Munk, W. (1975). Space-time scales of internal waves: A progress report. *Journal of Geophysical Research*, *80*(3), 291–297.

Giddy, I., Swart, S., du Plessis, M., Thompson, A., & Nicholson, S.-A. (2021). Stirring of sea-ice meltwater enhances submesoscale fronts in the southern ocean. *Journal of Geophysical Research: Oceans*, *126*(4), e2020JC016814.

Gille, S. T., Sheen, K. L., Swart, S., & Thompson, A. F. (2022). Mixing in the southern ocean. In *Ocean mixing* (pp. 301–327). Elsevier.

Haynes, P., & Anglade, J. (1997). The vertical-scale cascade in atmospheric tracers due to large-scale differential advection. *Journal of the atmospheric sciences*, *54*(9), 1121–1136.

Hosegood, P., Gregg, M. C., & Alford, M. H. (2006). Sub-mesoscale lateral density structure in the oceanic surface mixed layer. *Geophysical Research Letters*, *33*(22).

Ito, T., Follows, M., & Boyle, E. (2004). Is aou a good measure of respiration in the oceans? *Geophysical research letters*, *31*(17).

Jaeger, G. S., Lucas, A. J., & Mahadevan, A. (2020). Formation of interleaving layers in the bay of bengal. *Deep Sea Research Part II: Topical Studies in Oceanography*, *172*, 104717.

Jaeger, G. S., MacKinnon, J., Lucas, A., Shroyer, E., Nash, J., Tandon, A., ... Mahadevan, A. (2020). How spice is stirred in the bay of bengal. *Journal of Physical Oceanography*, *50*(9), 2669–2688.

Klymak, J. M., Crawford, W., Alford, M. H., MacKinnon, J. A., & Pinkel, R. (2015). Along-isopycnal variability of spice in the north pacific. *Journal of Geophysical Research: Oceans*, *120*(3), 2287–2307.

LaCasce, J., Ferrari, R., Marshall, J., Tulloch, R., Balwada, D., & Speer, K. (2014). Float-derived isopycnal diffusivities in the dimes experiment. *Journal of physical oceanography*, *44*(2), 764–780.

McCaffrey, K., Fox-Kemper, B., & Forget, G. (2015). Estimates of ocean macroturbulence: Structure function and spectral slope from argo profiling floats. *Journal of Physical Oceanography*, *45*(7), 1773–1793.

McDougall, T. J., & Barker, P. M. (2011). *Getting started with teos-10 and the gibbs seawater (gsw) oceanographic toolbox* (Vol. 37).

Morrison, A. K., Waugh, D. W., Hogg, A. M., Jones, D. C., & Abernathey, R. P. (2022). Ventilation of the southern ocean pycnocline. *Annual Review of Marine Science*, *14*, 405–430.

Naveira Garabato, A. C., MacGilchrist, G. A., Brown, P. J., Evans, D. G., Meijers, A. J., & Zika, J. D. (2017). High-latitude ocean ventilation and its role in earth's climate transitions. *Philosophical Transactions of the Royal Society A: Mathematical, Physical and Engineering Sciences*, *375*(2102), 20160324.

Ollitrault, M., Gabillet, C., & De Verdiere, A. C. (2005). Open ocean regimes of relative dispersion. *Journal of fluid mechanics*, *533*, 381–407.

Pietri, A., Testor, P., Echevin, V., Chaigneau, A., Mortier, L., Eldin, G., & Grados, C. (2013). Finescale vertical structure of the upwelling system off southern peru as observed from glider data. *Journal of Physical Oceanography*, *43*(3),

631–646.

Polzin, K., & Ferrari, R. (2004). Isopycnal dispersion in natre. *Journal of physical oceanography*, *34*(1), 247–257.

Prerau, M. J., Brown, R. E., Bianchi, M. T., Ellenbogen, J. M., & Purdon, P. L. (2017). Sleep neurophysiological dynamics through the lens of multitaper spectral analysis. *Physiology*, *32*(1), 60–92.

Roach, C. J., Balwada, D., & Speer, K. (2016). Horizontal mixing in the southern ocean from argo float trajectories. *Journal of Geophysical Research: Oceans*, *121*(8), 5570–5586.

Rossby, T., Omand, M., Palter, J., & Hebert, D. (2021). On rates of isopycnal dispersion at the submesoscale. *Geophysical Research Letters*, *48*(12), e2021GL093526.

Rudnick, D. L., & Ferrari, R. (1999). Compensation of horizontal temperature and salinity gradients in the ocean mixed layer. *Science*, *283*(5401), 526–529.

Rudnick, D. L., & Martin, J. P. (2002). On the horizontal density ratio in the upper ocean. *Dynamics of atmospheres and oceans*, *36*(1-3), 3–21.

Shcherbina, A. Y., Gregg, M. C., Alford, M. H., & Harcourt, R. R. (2009). Characterizing thermohaline intrusions in the north pacific subtropical frontal zone. *Journal of Physical Oceanography*, *39*(11), 2735–2756.

Siegelman, L. (2020). Energetic submesoscale dynamics in the ocean interior. *Journal of Physical Oceanography*, *50*(3), 727–749.

Siegelman, L., Klein, P., Rivière, P., Thompson, A. F., Torres, H. S., Flexas, M., & Menemenlis, D. (2020). Enhanced upward heat transport at deep submesoscale ocean fronts. *Nature Geoscience*, *13*(1), 50–55.

Smith, K., Boccaletti, G., Henning, C., Marinov, I., Tam, C., Held, I., & Vallis, G. (2002). Turbulent diffusion in the geostrophic inverse cascade. *Journal of Fluid Mechanics*, *469*, 13–48.

Smith, K. S., & Ferrari, R. (2009). The production and dissipation of compensated thermohaline variance by mesoscale stirring. *Journal of Physical Oceanography*, *39*(10), 2477–2501.

Stewart, K. D., & Haine, T. W. (2016). Thermobaricity in the transition zones between alpha and beta oceans. *Journal of Physical Oceanography*, *46*(6), 1805–1821.

Su, Z., Wang, J., Klein, P., Thompson, A. F., & Menemenlis, D. (2018). Ocean submesoscales as a key component of the global heat budget. *Nature communications*, *9*(1), 1–8.

Talley, L. D., Rosso, I., Kamenkovich, I., Mazloff, M. R., Wang, J., Boss, E., ... others (2019). Southern ocean biogeochemical float deployment strategy, with example from the greenwich meridian line (go-ship a12). *Journal of Geophysical Research: Oceans*, *124*(1), 403–431.

Tamsitt, V., Drake, H. F., Morrison, A. K., Talley, L. D., Dufour, C. O., Gray, A. R., ... others (2017). Spiraling pathways of global deep waters to the surface of the southern ocean. *Nature communications*, *8*(1), 1–10.

Thomas, J., & Yamada, R. (2019). Geophysical turbulence dominated by inertia–gravity waves. *Journal of Fluid Mechanics*, *875*, 71–100.

Thompson, A. F., & Sallée, J.-B. (2012). Jets and topography: Jet transitions and the impact on transport in the antarctic circumpolar current. *Journal of physical Oceanography*, *42*(6), 956–972.

Timmermans, M.-L., & Winsor, P. (2013). Scales of horizontal density structure in the chukchi sea surface layer. *Continental Shelf Research*, *52*, 39–45.

Tulloch, R., Ferrari, R., Jahn, O., Klocker, A., LaCasce, J., Ledwell, J. R., ... Watson, A. (2014). Direct estimate of lateral eddy diffusivity upstream of drake passage. *Journal of Physical Oceanography*, *44*(10), 2593–2616.

Vallis, G. K. (2017). *Atmospheric and oceanic fluid dynamics*. Cambridge University Press.

van Sebille, E., Waterman, S., Barthel, A., Lumpkin, R., Keating, S. R., Fogwill, C., & Turney, C. (2015). Pairwise surface drifter separation in the western pacific sector of the southern ocean. *Journal of Geophysical Research: Oceans*, *120*(10), 6769–6781.

Yu, X., Naveira Garabato, A. C., Martin, A. P., Buckingham, C. E., Brannigan, L., & Su, Z. (2019). An annual cycle of submesoscale vertical flow and restratification in the upper ocean. *Journal of Physical Oceanography*, *49*(6), 1439–1461.

Zika, J. D., Sallée, J.-B., Meijers, A. J., Naveira-Garabato, A. C., Watson, A. J., Messias, M.-J., & King, B. A. (2020). Tracking the spread of a passive tracer through southern ocean water masses. *Ocean Science*, *16*(2), 323–336.

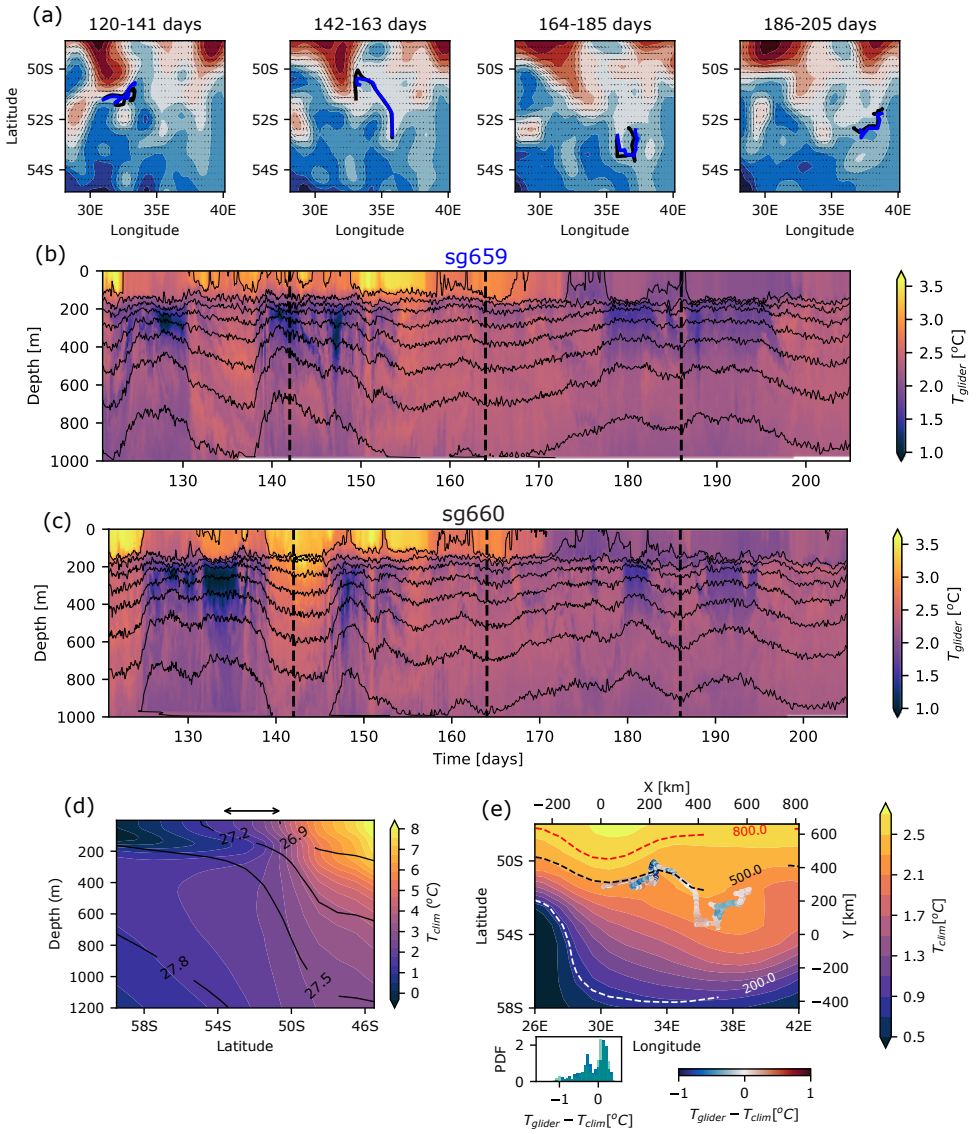

Figure 1. Glider tracks and sections relative to the sea surface height (SSH) and climatology. (a) Sea surface height and geostrophic velocity for four different periods during the glider deployment. Each panel shows a 3 week SSH average over the time period denoted in the titles. The glider tracks are shown as black (SG660) and blue (SG659) lines. (b), (c) Conservative temperature section for SG660 and SG659 respectively, plotted as a function of time (yearday for 2019). The potential density referenced to the surface is shown as black contour lines, with 0.1 kg m^{-3} as the contour levels. The vertical dashed black lines segment the panel into the four time periods that correspond to the four panels in (a). (d) Climatological mean temperature (color) and potential density surface (black contours) at 30°E, with the region sampled by the glider shown as black arrow on top. (e) Climatological mean temperature (color) on potential density surface 27.5, with the isopycnal depths shown using dashed contours. The glider path is colored to represent the temperature the glider observed on this isopycnal (T_{glider}) relative to the mean climatological temperature on this isopycnal (T_{clim}); the colorbar and PDF for $T_{glider} - T_{clim}$ is shown at the bottom of this panel.

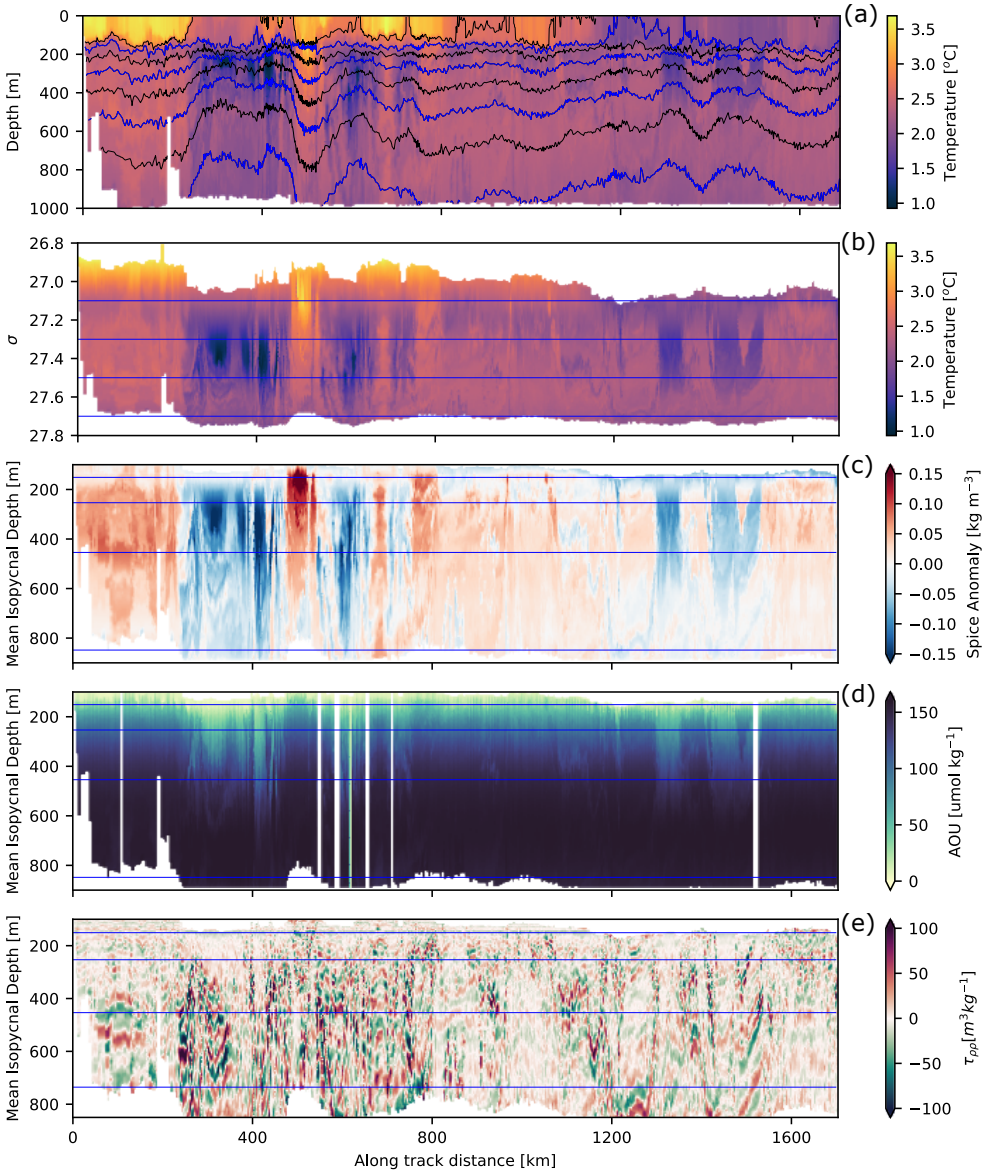

Figure 2. Sections from glider SG660 plotted as a function of along track distance. (a) Conservative temperature and isopycnals (potential density, black and blue contours with levels spaced by 0.1 kg m $^{-3}$) as a function of depth. (b) Conservative temperature as a function of isopycnal potential density. (c) Spice anomaly as a function of mean isopycnal depth. (d) Apparent oxygen utilization (AOU) as a function of mean isopycnal depth. (e) Diapycnal spice curvature, a metric to visually show layering, as a function of mean isopycnal depth. Horizontal blue lines in panels (b), (c), (d), and (e) indicate the mean depth of the 27.1, 27.3, 27.5, and 27.7 kg m $^{-3}$ potential density surfaces, which are shown as blue contour lines in (a). Note that the x-axis in these plots is along track distance, which is different from the yearday time shown in Figure 1. A similar plot for SG659 is present in the Supp. Info.

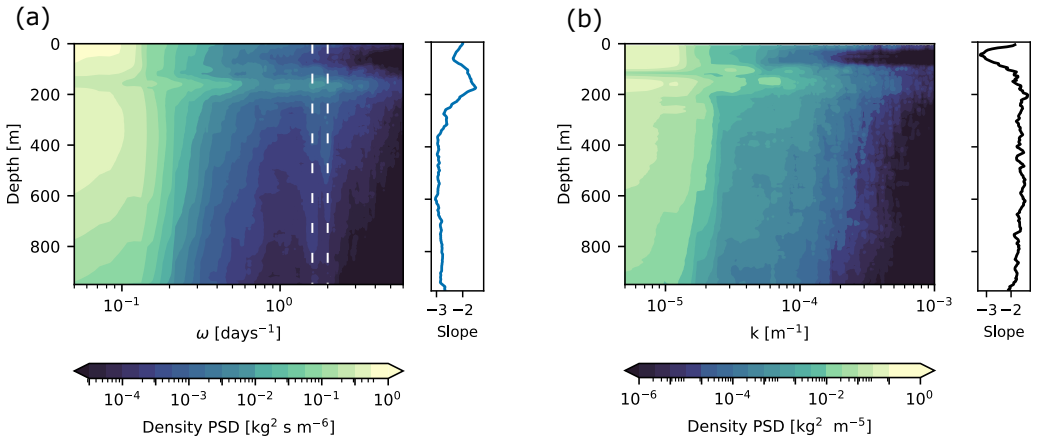

Figure 3. Density spectra at fixed depth. (a) Frequency power spectra of potential density, estimated at fixed depth, plotted as a function of depth. Vertical dashed lines denote the frequencies corresponding to the inertial frequency (15 hours) and semi-diurnal tide frequency (12 hours). (b) Wavenumber power spectra of potential density, estimated at fixed depth, plotted as a function of depth; the estimation for this figure was done using only the data from the relatively straight glider section in the middle of the sampling period. The glider timeseries were linearly interpolated to a 1 hour uniform time axis to do the frequency spectrum estimation and to 500 m uniform distance axis to do the wavenumber spectrum estimation. Slopes (α) corresponding to the power law (ω^α or k^α) of the power spectra between frequencies corresponding to 10 days and 18 hours (0.1 - 1.33 days^{-1} or wavenumbers corresponding to 50 km and 5 km (2×10^{-5} - 2×10^{-4} m^{-1}) are shown in the thin panels to the right of the main panels. The fitting range was chosen to avoid fitting the internal wave and tidal peaks in the frequency spectra and to avoid fitting the wavenumbers impacted by the gridding.

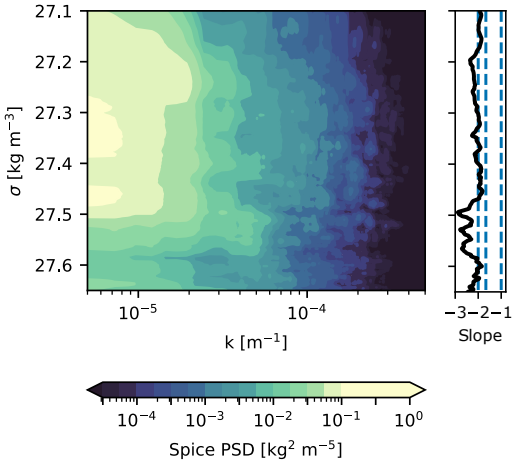

Figure 4. Spice spectra along isopycnals. Wavenumber power spectra of spice, estimated along isopycnals, plotted as a function of potential density. Slope corresponding to the power law of the power spectra between wavenumbers corresponding to scales of 50km to 5km is shown as thin panel to the right, where the range was chosen to avoid fitting the range of scales where linear interpolation to uniform grid and windowing from the multi-taper method impact the spectrum. The dashed blue lines in the slope plot correspond to slopes of -2, -5/3 and -1. The spectral estimation for this figure was done using only the data from the relatively straight glider section in the middle of the sampling period.

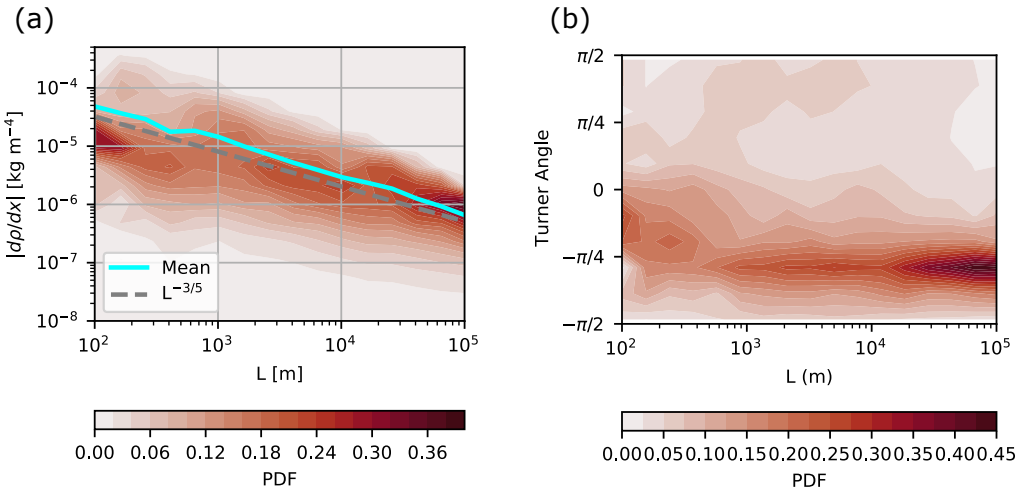

Figure 5. Mixed layer tracer structures. (a) Probability distribution function (PDF) of the absolute density gradient as a function of length scales, which is normalized separately for each length scale bin (integral over $|d\rho/dx|$ axis for each L is one). The cyan line corresponds to the mean of the PDF and the dashed gray line represents a power law with slope of $-3/5$, which provides a good visual fit over scales between 1-100km. (b) PDF of the Turner angle as a function of length scale.

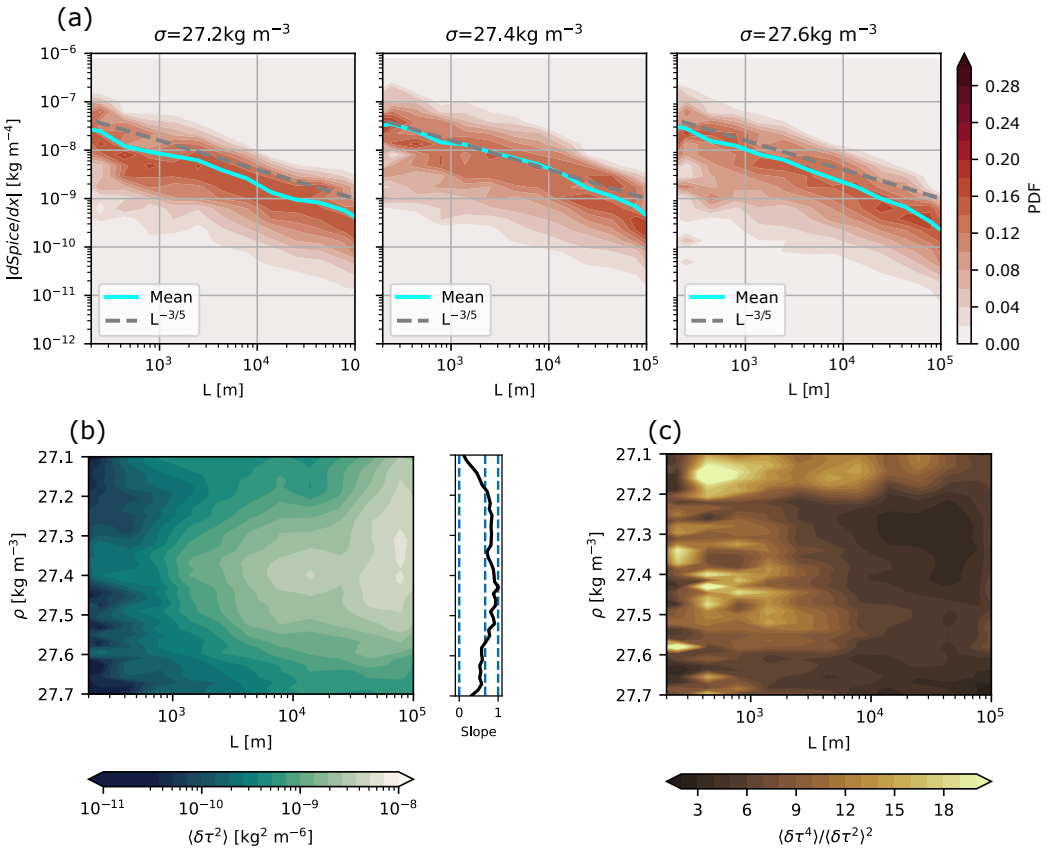

Figure 6. Along isopycnal tracer structures. (a) Probability distribution function of the absolute spice gradient as a function of length scale on different isopycnals (indicated in panel titles). The cyan line corresponds to the mean of the PDF and the dashed gray line represents a power law with slope of -3/5, which is the same in every panel for reference. (b) The 2^{nd} order structure function of along isopycnal spice plotted as a function of isopycnal and length scale. The slope of the 2^{nd} order SF on different isopycnals between scales of 700 m - 10 km is shown in the adjacent panel. Here the fitting range was chosen to avoid the noisy small scales and the large scales where 2^{nd} order SF starts to flatten, indicating the that the spice anomalies begin to decorrelate. In this panel showing the slope the dashed vertical lines correspond to slopes of 0, 2/3 and 1. (c) The normalized fourth order structure function (kurtosis) plotted as a function of isopycnal and length scale.

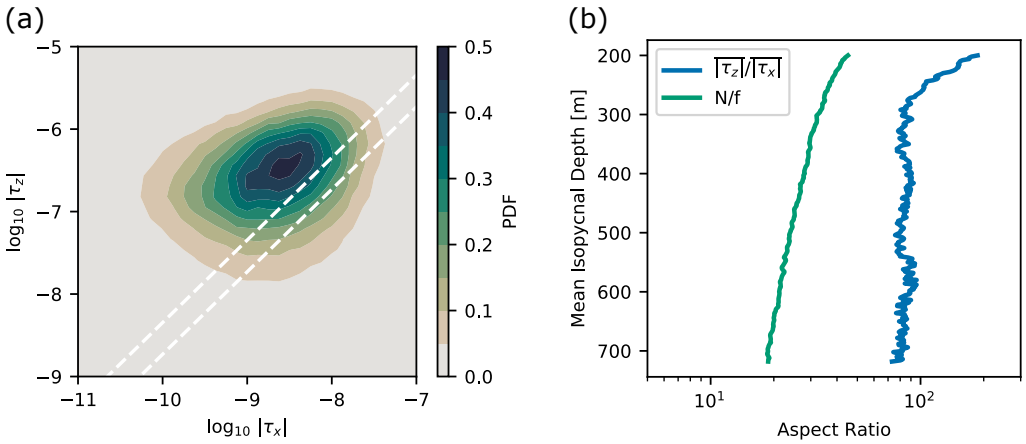

Figure 7. Slopes of spice filaments. (a) Probability distribution function of the absolute horizontal and vertical spice gradients for all the data between the mean isopycnal depth of 200-750 m, a range that extends from below the mixed layer to the mean isopycnal depth where sufficient data is available. The white lines correspond to the minimum and maximum aspect ratio that would be expected based on the range of observed N/f values (K. S. Smith & Ferrari, 2009). (b) The aspect ratio of the spice gradient, defined as the ratio of the mean absolute vertical spice gradient to the mean absolute horizontal spice gradient, and N/f as a function of mean isopycnal depth.

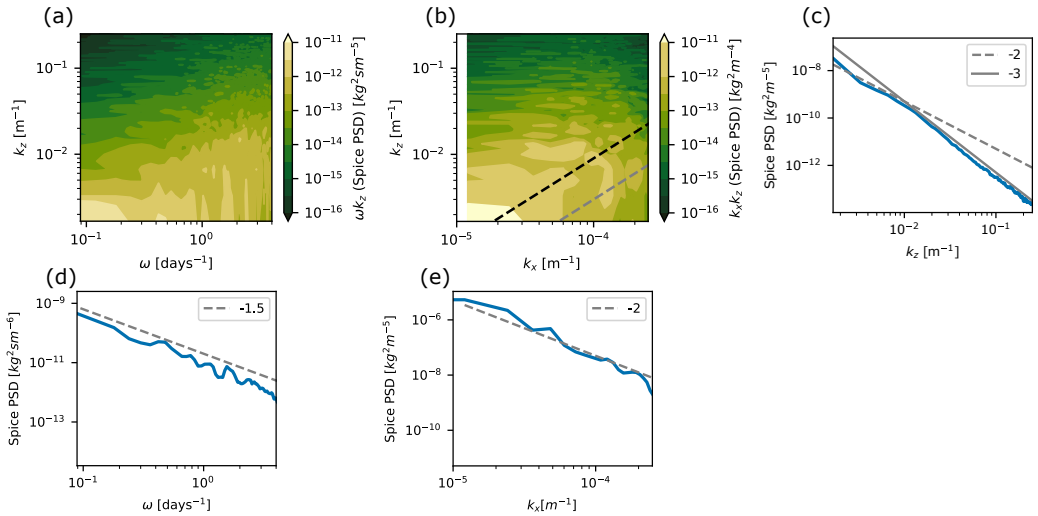

Figure 8. 2D spice power spectra (PSD). (a) Frequency vs vertical wavenumber (ω vs k_z) spice PSD in variance preserving form. (b) Horizontal wavenumber vs vertical wavenumber (k_x vs k_z) spice PSD in variance preserving form. The dashed gray line corresponds to structures that would follow an aspect ratio of N/f (vertical mean between 200-750m is 30), while the black dashed line corresponds to the observed aspect ratio (vertical mean between 200-750m is 90). (c) Spice PSD as a function of the vertical wavenumber, this panel is the integral of the frequency-vertical wavenumber PSD over all frequencies. The dashed line and dash-dotted line correspond to power law slopes of -2 and -3 respectively (d) Spice PSD as a function of the frequency, this panel is the integral of the frequency-vertical wavenumber PSD over all vertical-wavenumber. The dashed line corresponds to power law slope of -1.5. (e) Spice PSD as a function of the horizontal wavenumber, this panel is the integral of the horizontalwavenumber vs vertical wavenumber PSD over all vertical-wavenumber. The dashed line corresponds to power law slope of -2. The estimation in (b) and (e) was done using only the data from the relatively straight glider section in the middle of the sampling period, while panels (a), (c) and (d) was done using the entire dataset. Large frequencies and wavenumbers where the gridding artefacts dominate are not shown.

Figure 1.

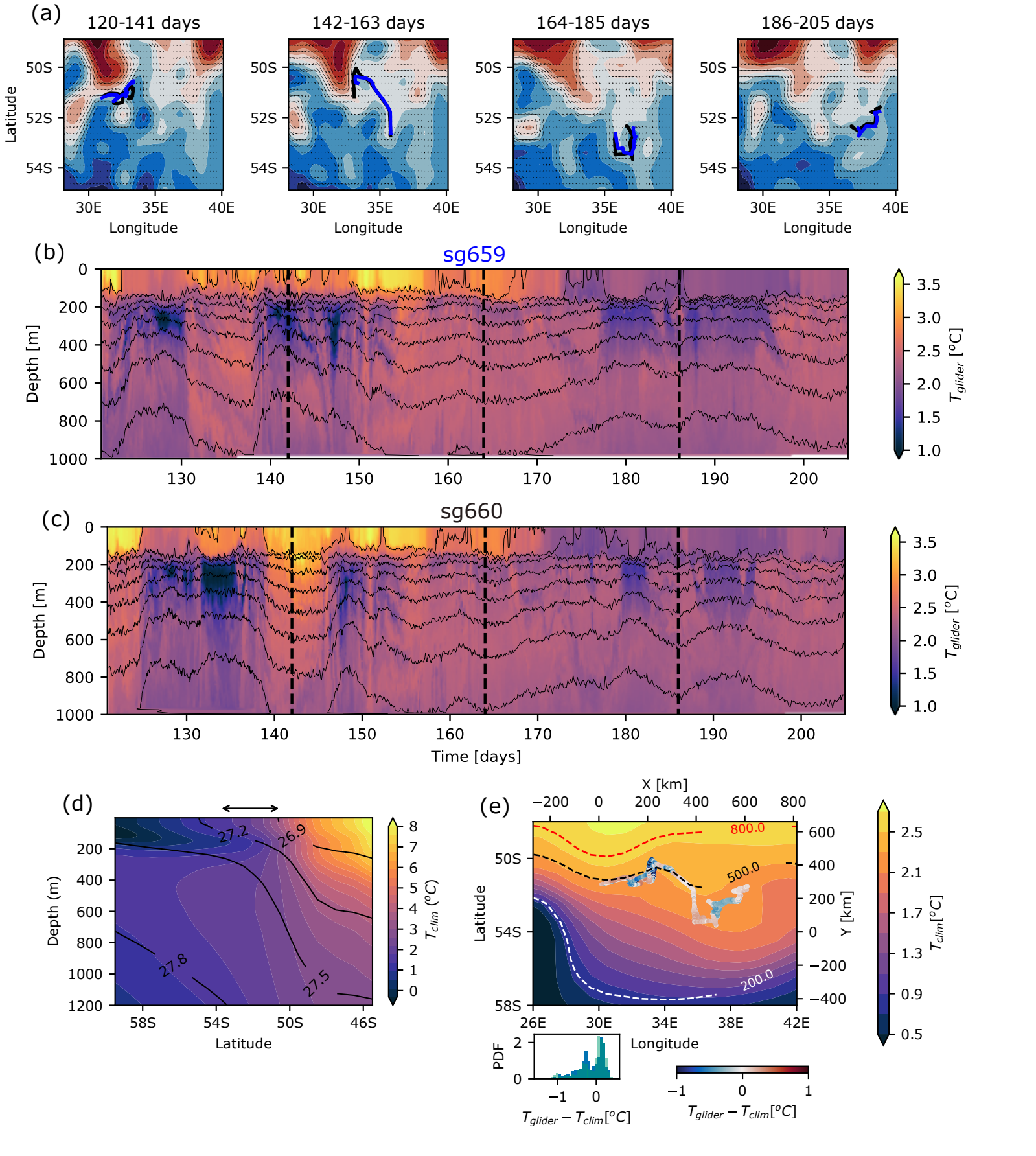
(a)
120-141 days
142-163 days
164-185 days
186-205 days
Latitude
50S
52S
54S
30E
35E
40E
Longitude
(b)
sg659
Depth [m]
0
200
400
600
800
1000
130
140
150
160
170
180
190
200
T_{glider} [°C]
3.5
3.0
2.5
2.0
1.5
1.0
(c)
sg660
Depth [m]
Time [days]
T_{glider} [°C]
(d)
Depth (m)
1200
27.2
26.9
27.8
27.5
58S
54S
50S
46S
Latitude
T_{clim} (°C)
8
7
6
5
4
3
2
1
0
(e)
X [km]
−200
0
200
400
600
800
800.0
500.0
200.0
Latitude
58S
26E
30E
34E
38E
42E
Longitude
Y [km]
600
400
200
0
−200
−400
PDF
2
0
−1
0
$T_{glider} - T_{clim}[°C]$
1
T_{clim}[°C]
2.5
2.1
1.7
1.3
0.9
0.5

Figure 2.

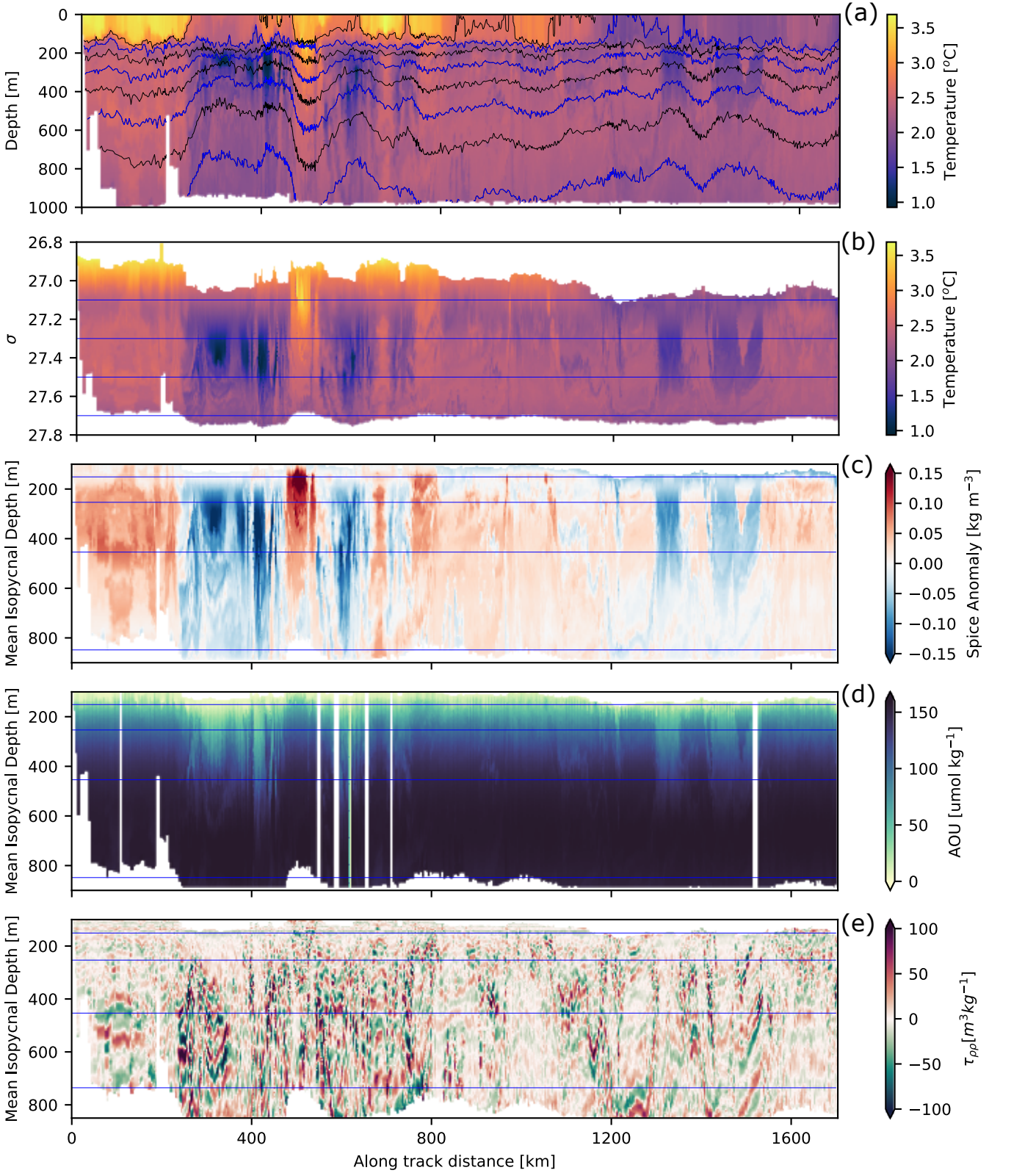
(a)
Depth [m]
0
200
400
600
800
1000
Temperature [°C]
3.5
3.0
2.5
2.0
1.5
1.0
(b)
σ
26.8
27.0
27.2
27.4
27.6
27.8
Temperature [°C]
(c)
Mean Isopycnal Depth [m]
Spice Anomaly [kg m⁻³]
0.15
0.10
0.05
0.00
−0.05
−0.10
−0.15
(d)
AOU [umol kg⁻¹]
150
100
50
0
(e)
$\tau_{\rho\rho}[m^3kg^{-1}]$
100
50
0
−50
−100
0
400
800
1200
1600
Along track distance [km]

Figure 3.

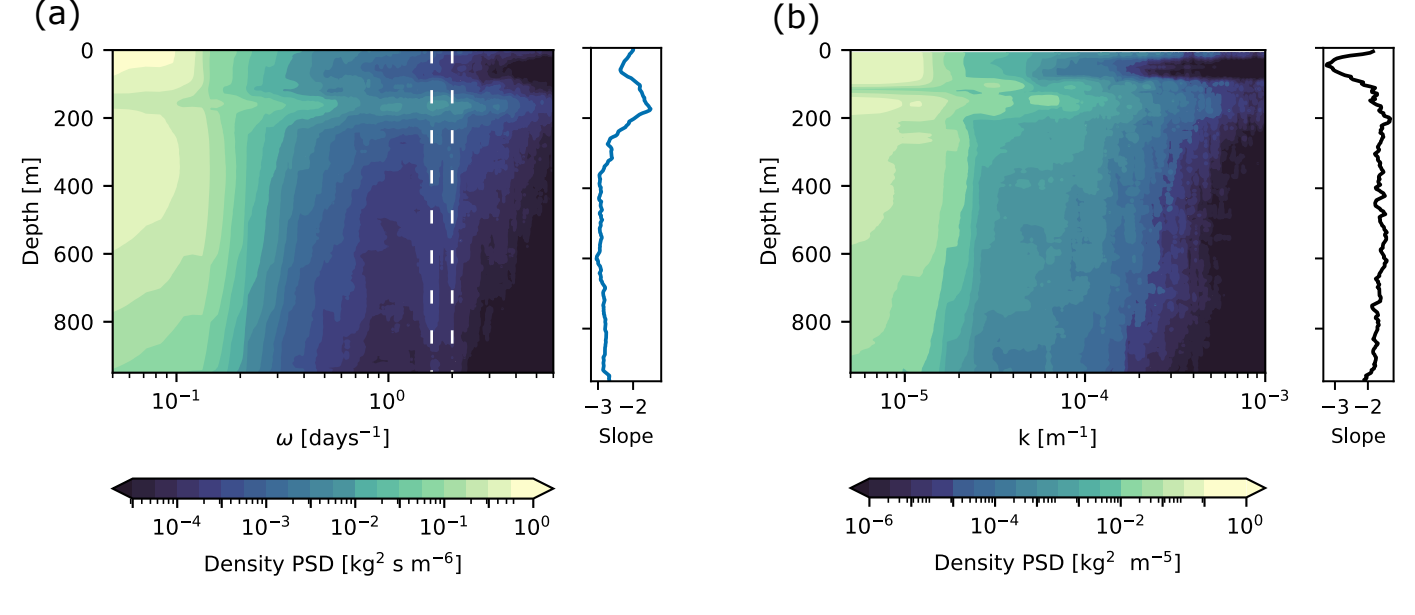
(a)
Depth [m]
0
200
400
600
800
10^{-1}
10^{0}
ω [days^{-1}]
−3 −2
Slope
10^{-4} 10^{-3} 10^{-2} 10^{-1} 10^{0}
Density PSD [kg^2 s m^{-6}]
(b)
Depth [m]
0
200
400
600
800
10^{-5}
10^{-4}
10^{-3}
k [m^{-1}]
−3 −2
Slope
10^{-6} 10^{-4} 10^{-2} 10^{0}
Density PSD [kg^2 m^{-5}]

Figure 4.

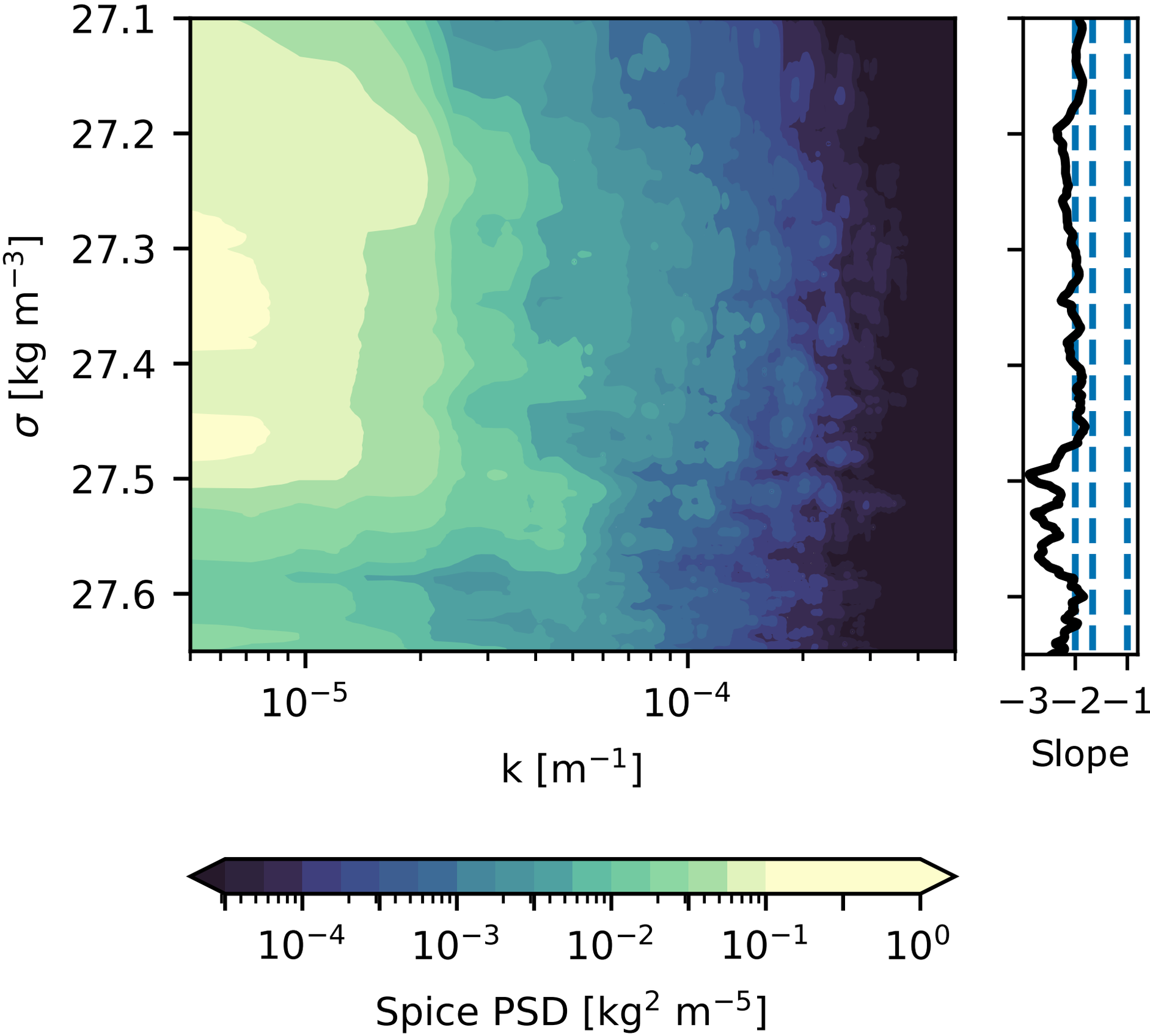
27.1
27.2
27.3
27.4
27.5
27.6
σ [kg m^{-3}]
10^{-5}
10^{-4}
k [m^{-1}]
−3
−2
−1
Slope
10^{-4}
10^{-3}
10^{-2}
10^{-1}
10^{0}
Spice PSD [kg^2 m^{-5}]

Figure 5.

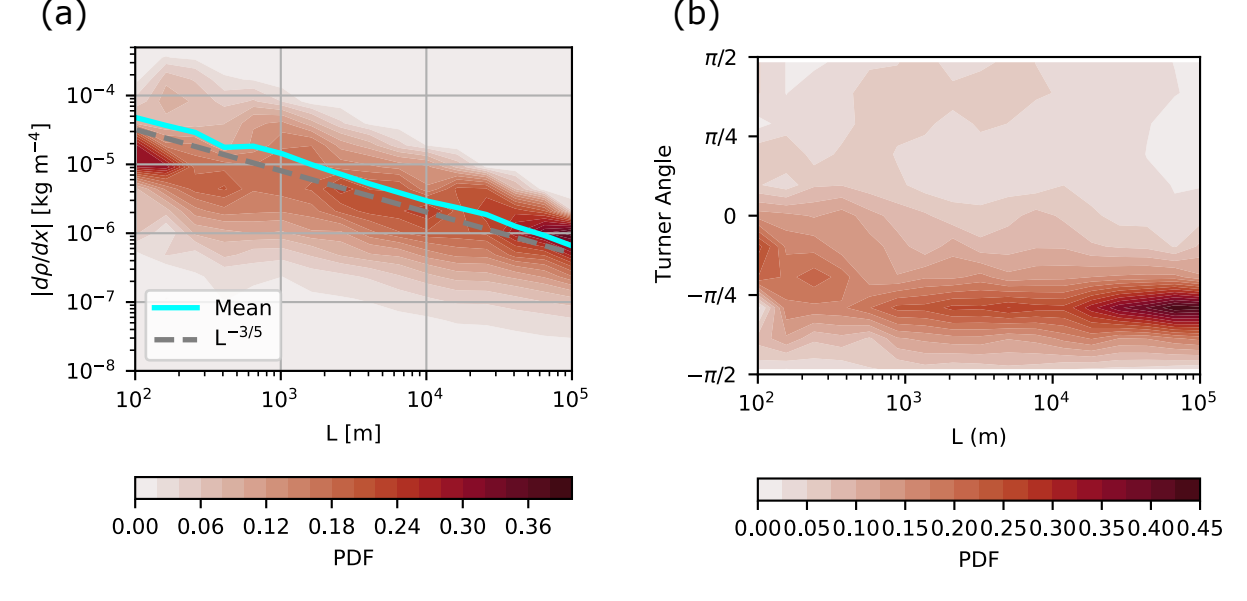
(a)
10^{-4}
10^{-5}
10^{-6}
10^{-7}
10^{-8}
$|d\rho/dx|$ [kg m^{-4}]
Mean
$L^{-3/5}$
10^2
10^3
10^4
10^5
L [m]
0.00 0.06 0.12 0.18 0.24 0.30 0.36
PDF
(b)
$\pi/2$
$\pi/4$
0
$-\pi/4$
$-\pi/2$
Turner Angle
10^2
10^3
10^4
10^5
L (m)
0.000.050.100.150.200.250.300.350.400.45
PDF

Figure 6.

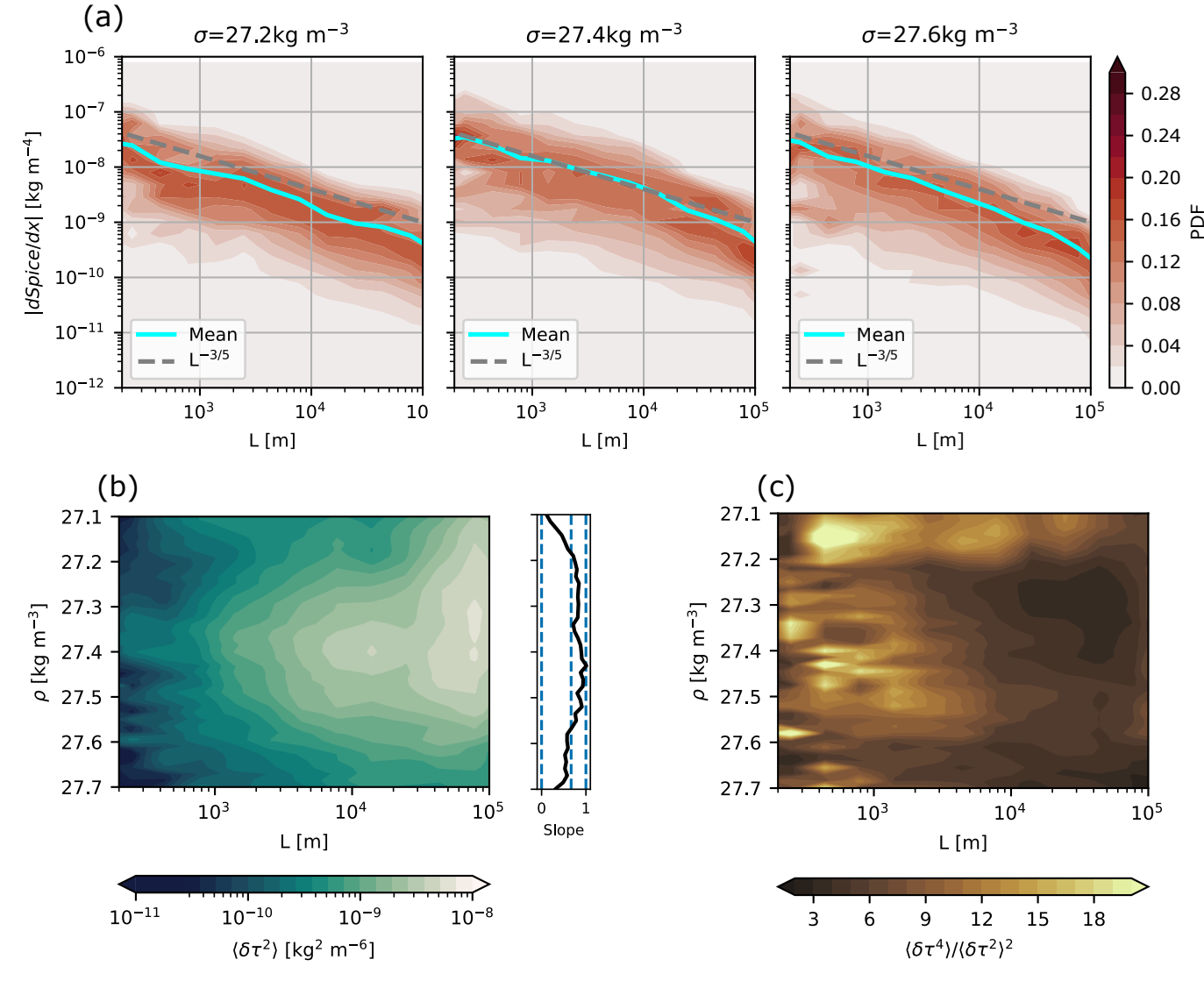
(a)
σ=27.2kg m−3
σ=27.4kg m−3
σ=27.6kg m−3
|dSpice/dx| [kg m−4]
Mean
L−3/5
L [m]
PDF
(b)
ρ [kg m−3]
Slope
⟨δτ2⟩ [kg2 m−6]
(c)
⟨δτ4⟩/⟨δτ2⟩2

Figure 7.

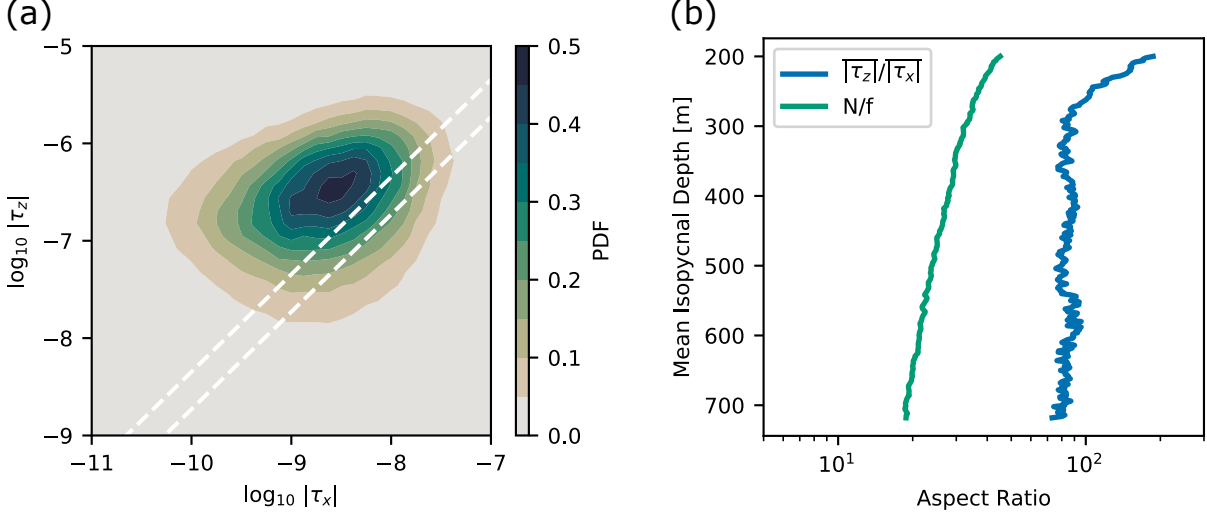
(a)
−5
−6
−7
−8
−9
log10 |τz|
−11
−10
−9
−8
−7
log10 |τx|
0.5
0.4
0.3
0.2
0.1
0.0
PDF
(b)
200
300
400
500
600
700
Mean Isopycnal Depth [m]
|τz|/|τx|
N/f
10^1
10^2
Aspect Ratio

Figure 8.

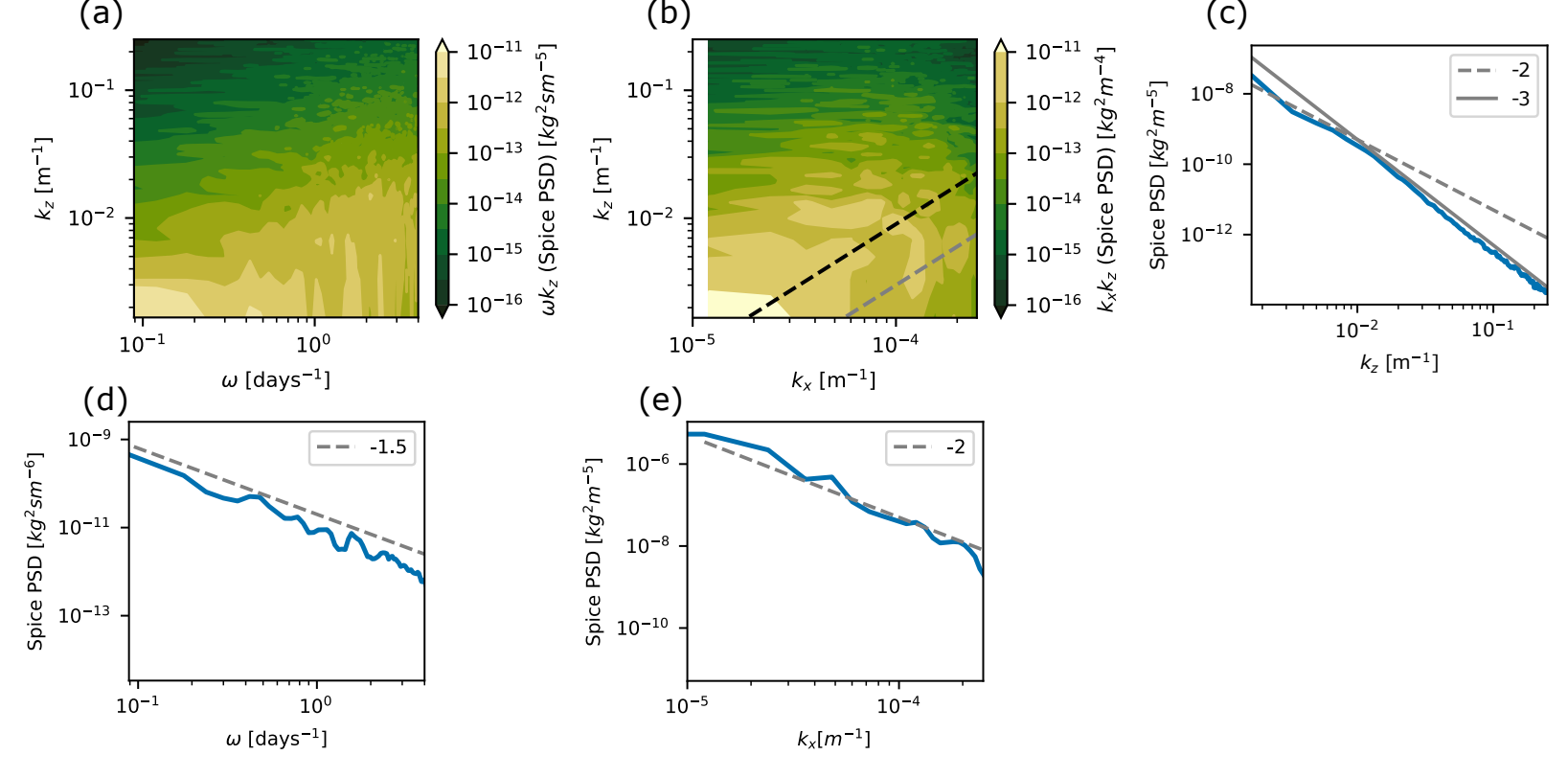
(a)
(b)
(c)
(d)
(e)
k_z [m^{-1}]
ω [days^{-1}]
ωk_z (Spice PSD) [kg^2sm^{-5}]
k_x [m^{-1}]
$k_x k_z$ (Spice PSD) [kg^2m^{-4}]
Spice PSD [kg^2m^{-5}]
-2
-3
Spice PSD [kg^2sm^{-6}]
-1.5